

## Research Article

## B isotopes reveal Eocene mélange melting in northern Tibet during continental subduction



Lin Ma <sup>a,b,c</sup>, Guo-Ning Gou <sup>a</sup>, Andrew C. Kerr <sup>c</sup>, Qiang Wang <sup>a,b,d,\*</sup>, Gang-Jian Wei <sup>a,b</sup>, Jin-Hui Yang <sup>e</sup>, Xiao-Ming Shen <sup>a,f</sup>

<sup>a</sup> State Key Laboratory of Isotope Geochemistry, Guangzhou Institute of Geochemistry, Chinese Academy of Sciences, Guangzhou 510640, China

<sup>b</sup> CAS Centre for Excellence in Deep Earth Sciences, Guangzhou 510640, China

<sup>c</sup> School of Earth and Environmental Sciences, Cardiff University, Cardiff, Wales CF10 3AT, United Kingdom

<sup>d</sup> College of Earth and Planetary Sciences, University of Chinese Academy of Sciences, Beijing 100049, China

<sup>e</sup> Institute of Geology and Geophysics, Chinese Academy of Science, Beijing 100029, China

<sup>f</sup> National Institute of Natural Hazards, Ministry of Emergency Management of China, Beijing 100085, China

## ARTICLE INFO

## Article history:

Received 14 September 2020

Received in revised form 30 March 2021

Accepted 31 March 2021

Available online 2 April 2021

## ABSTRACT

Continental subduction is an important but poorly known means of transporting the Earth's crust into the mantle. Continental subduction has also been proposed to be responsible for the formation of the Cenozoic intracontinental potassic rocks widespread in Tibet and uplift of the Tibetan Plateau. However, such ancient continental subduction only occasionally been identified and is controversial. In this contribution, we explore the use of boron and its isotopes, to provide new constraints on the origin of newly identified Eocene potassium-rich volcanic rocks in northern Tibet and potential subduction of continental crust. Our results indicate that the latest Eocene (ca. 34 Ma) potassium-rich volcanic rocks are characterised by moderate silica, adakite-like trace elements, enriched Sr-Nd-Pb and light boron isotope ( $\delta^{11}\text{B} = -20.12\% \text{ to } -7.95\%$ ) signatures. This isotopically light signature of boron suggests a mélange source composed of mantle wedge peridotite and recycled dehydrated continental crust. The Eocene potassium-rich magmas were likely derived from low-degree partial melting of diapir mélange at high-pressure and medium temperature within subduction channel. Our work indicates potential obduction of the Tibetan plate over the Asian plate thus triggering intracontinental subduction before the end of Eocene. This continental obduction may have accommodated a huge amount of crustal material during Cenozoic rapid convergence between India and Asia. We conclude that during this process an isotopically light component is likely to have been transported into the mantle to form a distinct source region. B isotopes therefore have the potential to trace the continental crust recycling in large collisional orogens.

© 2021 Elsevier B.V. All rights reserved.

## 1. Introduction

Subduction zones are crucial for understanding element cycling within Earth because they transport oceanic basalt, seafloor sediment and fragments of continental crust to mantle depths (e.g., Hermann et al., 2013; Stern, 2002). Element cycling through oceanic subduction zones is well established, but these processes in continental subduction zones poorly understood due to a lack of mantle-derived magmatism during continental subduction and the information it carries (Collins et al., 2011). In addition, subduction of continental crust is thought to be difficult and rare due to lower density than the mantle. However, crustal mass balance calculations in the India–Asia collisional system indicate that half of the pre-collisional continental crustal mass since 56

million years ago, is likely to have been transported into the mantle (Ingalls et al., 2016). The Tibetan Plateau therefore offers an excellent opportunity to trace these crustal materials and their impact on mantle geochemistry (Ingalls et al., 2016; Liu and Rudnick, 2011).

The Tibetan Plateau was formed by the accretion of multi-terrane and subsequent continental collision and potential continental subduction (Chung et al., 2005; Tappognon et al., 2001; Yin and Harrison, 2000). Uplift of the plateau has significantly influenced the surface of the Earth and affected the Cenozoic climate system (Dupont-Nivet et al., 2007; Royden et al., 2008). However, the role of continental subduction in surface uplift and evolution of the Tibetan Plateau remains highly controversial (Kind et al., 2002; Tappognon et al., 2001; Zhao et al., 2010) and lithosphere thinning or delamination is regarded as the dominant mechanism of plateau uplift (Chen et al., 2017; Turner et al., 1993).

Cenozoic potassium-rich magmatism with enriched incompatible elements and Sr-Nd isotope signatures are widespread in the centre of the

\* Corresponding author at: State Key Laboratory of Isotope Geochemistry, Guangzhou Institute of Geochemistry, Chinese Academy of Sciences, Guangzhou 510640, China.

E-mail address: [wqiang@gig.ac.cn](mailto:wqiang@gig.ac.cn) (Q. Wang).

Tibetan plateau (Chung et al., 2005; Ding et al., 2003; Guo et al., 2006; Wang et al., 2008), 300–600 km north of the collision boundary. Such lavas with characteristic geochemical compositions have been proposed to form due to continental crust subduction (Guo et al., 2006, 2014, 2015; Ma et al., 2017). Alternatively, the delamination model suggests the potassium-rich lava was derived from enriched lithospheric mantle that was formed during ancient oceanic subduction (Chung et al., 1998; Turner et al., 1996), prior to continental subduction (Chung et al., 2005). The study of the origin of Cenozoic potassic rocks in the Tibetan Plateau provides an excellent opportunity to assess the likelihood of continental subduction and its potential impact on mantle geochemistry. In this contribution, we explore the use of boron, and its isotopes ( $^{10}\text{B}$  and  $^{11}\text{B}$ ), to constrain causal connections between the origin of post-collisional potassium-rich magmatism and continental crust cycling.

## 2. Geological backgrounds

The assembly of Tibetan Plateau was the result of the accretion of a series of Gondwana-derived terranes onto the Asian continental margin during the Mesozoic to Cenozoic (Yin and Harrison, 2000). From north to south, the main east–west-trending blocks are the Songpan-Ganze, Qiangtang, Lhasa and Himalaya Blocks (Fig. 1) (Chung et al., 2005; Yin and Harrison, 2000), that are separated from each other by the Jinsha, Bangong–Nujiang and Indus–Yarlung Tsangpo sutures (Fig. 1), representative relicts of the Paleo-, Meso- and Neo-Tethys, respectively.

The Qiangtang Block is located in the centre of Tibetan Plateau (Fig. 1). After the closure of the Meso-Tethys with the collision between the Qiangtang and Lhasa Blocks during the Early Cretaceous (ca. 160–100 Ma), there was very little magmatism in the Qiangtang block during the Late Cretaceous (Peng et al., 2020; Xu et al., 2020; Zhu et al., 2013). Cenozoic igneous rocks are sporadically distributed in the Qiangtang but are mainly clustered in the northern part of the block close to the Jinsha suture (Fig. 1). The late Jurassic to Eocene (ca. 148–45 Ma) Na-rich alkali basalts occur in the northwestern Qiangtang Block (e.g., Deng, 1998; Ding et al., 2003; Ma et al., 2021), while Eocene–early Oligocene (ca. 45–23 Ma) volcanic and subordinate intrusive rocks are widely distributed throughout the Block (Fig. 1) (e.g., Chung et al., 2005; Guo et al., 2006; Ou et al., 2019; Yakovlev et al., 2019). Eocene (ca. 50–36 Ma) magmatic rocks consist of high-K calc-alkaline lavas and intrusive rocks with minor shoshonitic lavas (Wang et al., 2008, 2010; Yakovlev et al., 2019), while the late early Oligocene (ca. 30–28 Ma) potassic lavas mainly comprise trachyandesites (Ding et al., 2003; Guo et al., 2006; Ou et al., 2019). Some Pliocene–Quaternary (4.7–2.3 Ma) felsic lavas (Wang et al., 2016) and Miocene to present (8.3–0 Ma) mafic potassic rocks (Guo et al., 2014) have also been reported from the northern Qiangtang Block (Fig. 1a).

Our study area is over ~900 km<sup>2</sup> and is located in the centre of the plateau about 100 km northwest of Tuotuohe town, at an altitude of 5000 m and adjacent to the Jinsha suture zone (Fig. 1a). In the area, the trachyte and trachy-andesite crop out along a 50 km<sup>2</sup> section of the River Zhamuqu (Fig. 1b) and overlie the lacustrine deposits of the upper Cretaceous Fenghuoshan Group and the Eocene Yaxico Formation. The distribution of these greyish white and porphyritic volcanics is controlled by NW–NE trending faults (Fig. 1b). The samples in this study were collected around the Yegai area (Fig. 1b) and contain ~25 vol% phenocrysts. These phenocrysts consist of euhedral high Ba-Sr alkali feldspar ( $\text{Ba-Sr}_{3-14}\text{An}_{1-7}\text{Ab}_{32-48}\text{Or}_{42-66}$ ; BaO up to 4.3 wt%), oligoclase plagioclase ( $\text{An}_{18-26}\text{Ab}_{65-76}\text{Or}_{5-11}$ ), biotite and quartz with small amounts of amphibole (Fig. 2). The groundmass is cryptocrystalline and made up of K-feldspar, plagioclase and minor quartz and oxide. The accessory minerals are mainly epidote, apatite, zircon and titanite.

## 3. Analytical methods

Cathodoluminescence (CL) imaging of zircon was performed at the State Key Laboratory of Isotope Geochemistry (SKLaBIG),

Guangzhou Institute of Geochemistry Chinese Academy of Sciences (GIG CAS). Two trachyandesite and three trachyte samples were selected for zircon U-Pb dating. An Agilent 7500a quadruple (Q)-ICPMS (Inductively Coupled Plasma Mass Spectrometry) and a Neptune multi-collector (MC)-ICPMS with a 193 nm excimer ArF laser-ablation system (GeoLas Plus) were used for simultaneous determination of zircon U-Pb ages at the Institute of Geology and Geophysics (IGG) CAS in Beijing. Zircon U-Pb isotopic data are given in Table S1. During the analyses in this study, the standard zircon 91,500 yielded a weighted  $^{206}\text{Pb}/^{238}\text{U}$  age of  $1062.5 \pm 3.8$  Ma ( $2\sigma$ , MSWD = 0.025, n = 52), which is consistent with the data of 1065 Ma reported by Wiedenbeck et al. (1995).

Rock samples were first examined by optical microscopy and the freshest whole-rock samples were broken into small chips. These chips were cleaned ultrasonically in distilled water containing <3% HNO<sub>3</sub> and washed with distilled water before being dried and handpicked to remove visible contamination. The rocks were powdered before analysis of major and trace elements, and Sr-Nd-Pb-B isotopes at SKLaBIG GIG CAS. The major and trace elements data are given in Table S2. Major-element oxides were determined by a Rigaku RIX 2000 X-ray fluorescence spectrometer on fused glass beads with analytical uncertainties <5% (Table S3). Trace elements were analysed by a Perkin-Elmer ScieX ELAN 6000 instrument. Trace element data of reference materials (BHVO-2, AGV-2, BCR-2 and RGM-2), blank and replicate analyses are given in Tables S3–S4.

Sr, Nd and Pb isotopic compositions of selected samples were determined using a MC-ICPMS at SKLaBIG, GIG-CAS. The  $^{87}\text{Sr}/^{86}\text{Sr}$  ratio of the NBS987 standard and  $^{143}\text{Nd}/^{144}\text{Nd}$  ratio of the Shin Etsu JNd-1 standard measured were  $0.710284 \pm 4$  ( $2\sigma$ , n = 30) and  $0.512093 \pm 3$  ( $2\sigma$ , n = 17), respectively. All measured  $^{143}\text{Nd}/^{144}\text{Nd}$  and  $^{86}\text{Sr}/^{88}\text{Sr}$  ratios are fractionation corrected to  $^{146}\text{Nd}/^{144}\text{Nd} = 0.7219$  and  $^{86}\text{Sr}/^{88}\text{Sr} = 0.1194$ , respectively. The NBS981 as the standard sample yielded the  $^{206}\text{Pb}/^{204}\text{Pb}$ ,  $^{207}\text{Pb}/^{204}\text{Pb}$ ,  $^{208}\text{Pb}/^{204}\text{Pb}$  ratios were  $16.9363 \pm 0.0001$  ( $2\sigma$ , n = 20),  $15.4873 \pm 0.0001$  ( $2\sigma$ , n = 20), and  $36.6773 \pm 0.0004$  ( $2\sigma$ , n = 20), respectively.

B abundance and B isotopic analyses were conducted in SKLaBIG, GIG-CAS. The details of boron extraction and analytical procedures of B and  $\delta^{11}\text{B}$  are described by Wei et al. (2013). About 150 mg of bulk rock powder, along with 100  $\mu\text{l}$  1% mannitol, 100  $\mu\text{l}$  H<sub>2</sub>O<sub>2</sub> and 1 ml 24 M HF, was precisely weighed into a pre-cleaned 7 ml PFA-Teflon beaker. After reacting at <60 °C for 3 days and centrifugation, the supernatant was collected, and boron was concentrated in this solution, at a recovery of >99% (Wei et al., 2013). Boron was then separated by using a single column filled with AG MP anion resin in HF solution (Wei et al., 2013). A Varian Vista Pro inductively coupled plasma atomic emission spectrometer (ICP-AES) equipped with an HF-resistant Teflon spray chamber and an Al<sub>2</sub>O<sub>3</sub> injector was used for boron concentration measurement. Boron was measured using the 249.678 nm spectral line. Our column procedure separates Fe from B, so the large Fe spectral interference at 249.650 nm was minimized, which improved the effective detection limit to less than 0.01 ppm B in solution, enabling measurement of boron concentrations at <1 ppm in basalts. Internal precision for our boron concentration determinations were generally better than 5% (RSD). Basalt standards B-5 was measured multiple times as unknowns with our samples, yielding B concentrations of  $10.2 \pm 0.04$  ppm (1SD, n = 3), consistent with the long-time monitoring value of 10.18 ppm B in our laboratory.  $\delta^{11}\text{B}$  measurements were performed using a Finnegan Neptune MC-ICPMS in sample-standard bracketing (SSB) mode. The internal precision for  $\delta^{11}\text{B}$  was better than  $\pm 0.05\%$  ( $2\sigma$  standard error), and the external precision for  $\delta^{11}\text{B}$  was better than  $\pm 0.30\%$  ( $2\sigma$  standard error) estimated by the long-term results of SRM 951 (Wei et al., 2013). Several basalt standards such as B5, JB-2 and JB-3 were repeatedly analysed along with the samples, yielding the  $\delta^{11}\text{B}$  results of  $-4.36 \pm 0.04\%$  (1SD, n = 3),  $7.62 \pm 0.04\%$  (1SD, n = 3) and  $6.29 \pm 0.04\%$  (1SD, n = 4).

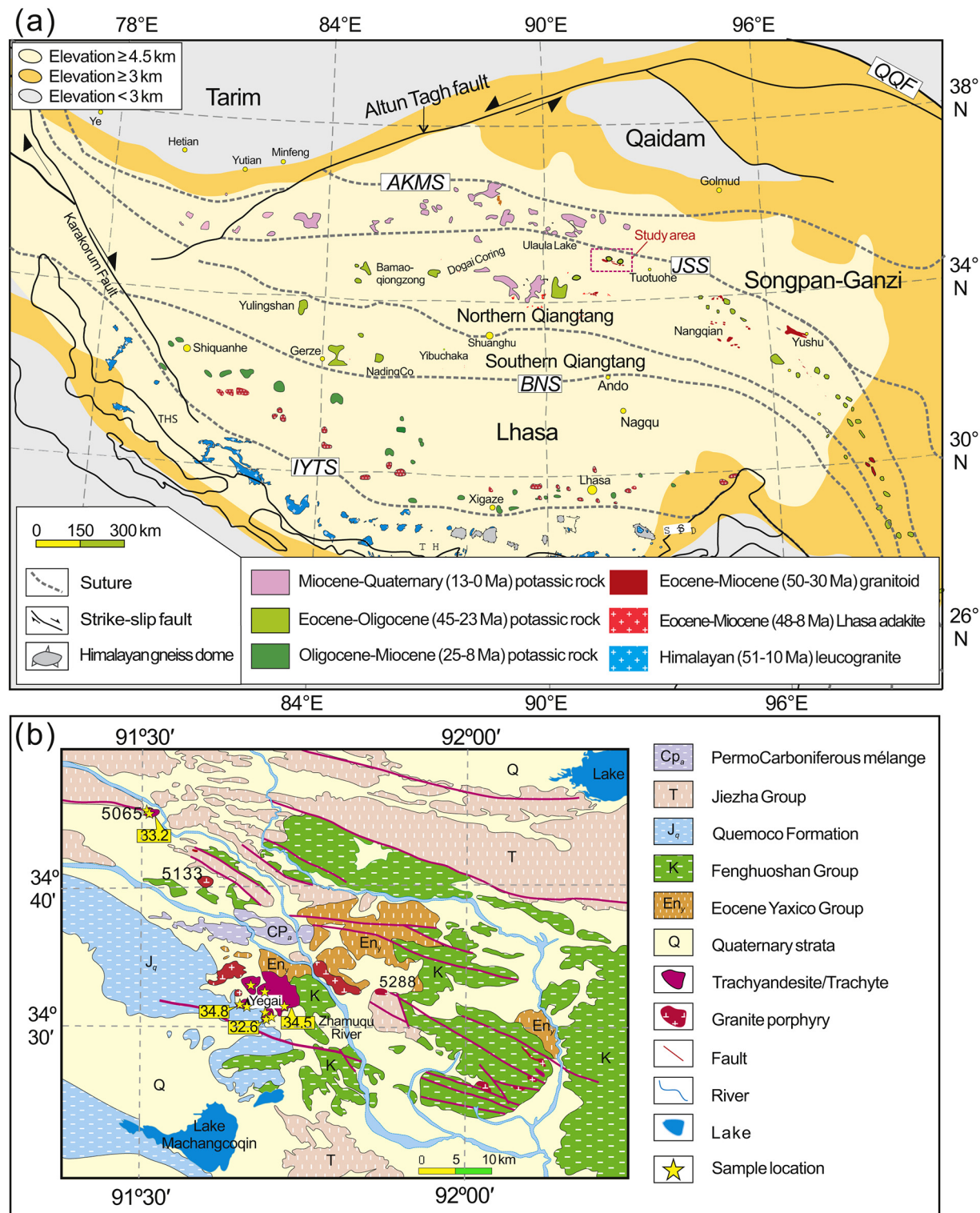


**Fig. 1.** (a) The post-collisional magmatic rocks in the Tibetan Plateau (modified from Chung et al., 2005). Abbreviations: IYTS – Indus-Yarlung Tsampo suture; BNS – Bangong-Nujiang suture; JSS – Jin-Sha suture; AKMS – Anymaqen-Kunlun-Muztagh Suture; QGF – Qilian-Qinling fault; STDS – South Tibet Detachment System; TH – Tethyan Himalaya. (b) Geological map of study area showing the distribution of the potassic volcanic rocks.

## 4. Results

### 4.1. Zircon U-Pb dating

High Th/U ratios (0.24–2.58) of zircons from the Yegai samples indicate a magmatic origin (Hoskin and Black, 2000). With the exception of some older dates of 235–59 Ma for inherited zircons,

the other U-Pb spot analyses from five samples yielded weighted-mean ages of  $34.1 \pm 0.5$  Ma (MSWD = 1.8),  $33.7 \pm 0.6$  Ma (MSWD = 2.0),  $33.9 \pm 0.5$  Ma (MSWD = 1.5),  $34.3 \pm 0.5$  Ma (MSWD = 2.5), and  $33.1 \pm 0.4$  Ma (MSWD = 0.78) (Fig. 3). These relatively consistent ages indicate that the Yegai trachyandesites and trachytes were emplaced in the latest Eocene to the earliest Oligocene.

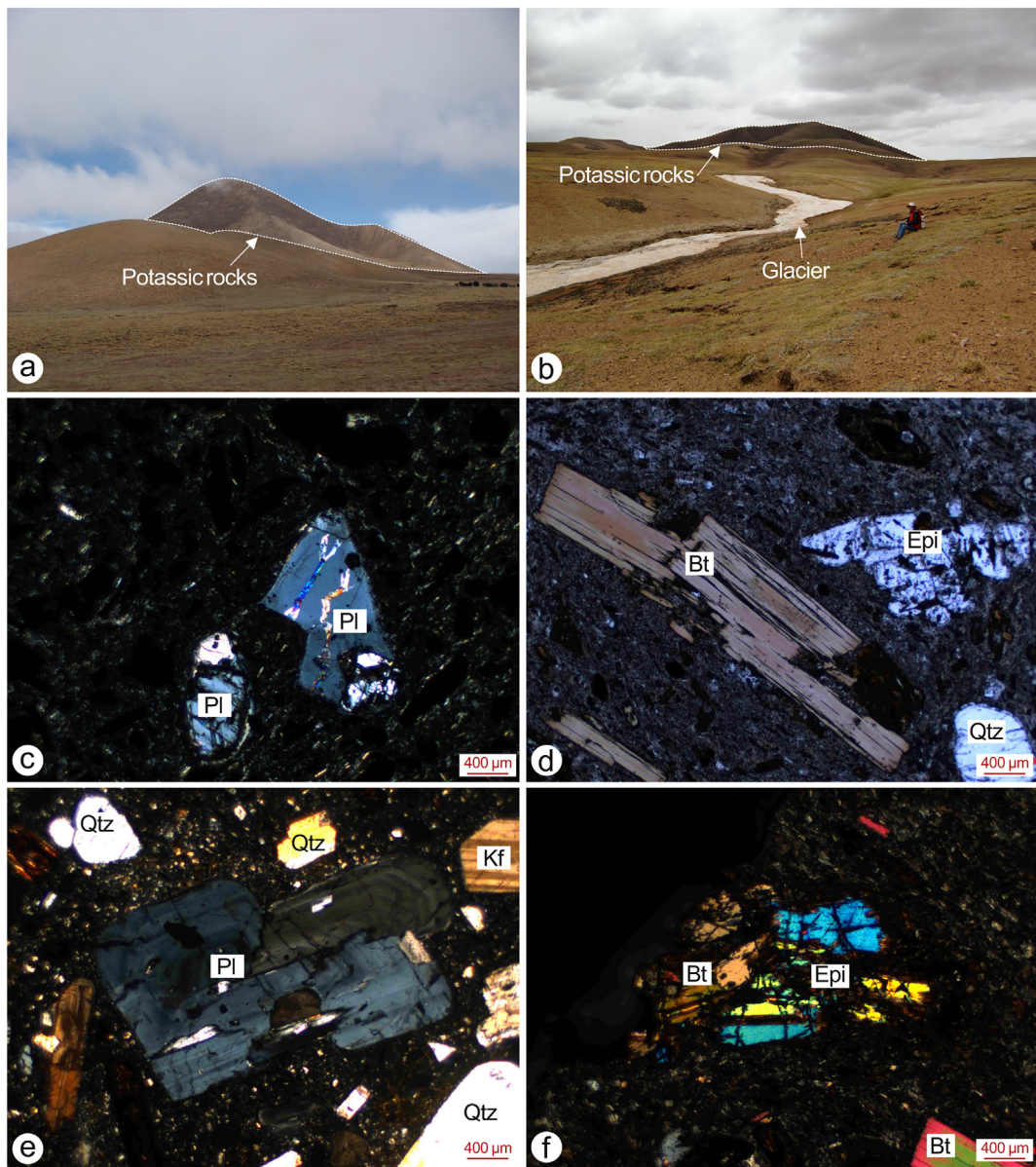


**Fig. 2.** Field and Petrographic photographs. (a, b) The field photos showing outcrop condition of potassic rocks. (c-f) cross-polarised petrographic photomicrographs showing porphyritic structure and major phenocrysts minerals. Abbreviation: Bt-biotite, Pl-plagioclase, Kf-potassium feldspar, Qtz-quartz; Epi-epidote.

#### 4.2. Major and trace elements

Data for 28 samples collected from the study area shows that the Yegai rocks are of trachyandesite and trachyte composition (Fig. 4a), with shoshonitic and ultrapotassic geochemical characteristics (Fig. 4b, c). These rocks are therefore very different from the potassic to high-K calc-alkaline geochemical features observed in modern arc lavas from active continental margins along the circum-Pacific subduction zone (Stern, 2002; Tatsumi and Eggins, 1995). The Late Paleogene Yegai rocks comprise two broad groups (1) a low-Mg suite ( $\text{SiO}_2 = 54.2\text{--}67.5\text{ wt\%}$  and  $\text{MgO} = 0.1\text{--}1.8\text{ wt\%}$ ) and (2) a moderate-Mg suite ( $\text{SiO}_2 = 56.8\text{--}62.7\text{ wt\%}$  and  $\text{MgO} = 2.4\text{--}3.6\text{ wt\%}$ ) (Fig. 4; Table S2).

The Yegai volcanic rocks are characterised by enriched light rare earth element (LREE) with a slight Eu anomaly ( $\text{Eu}/\text{Eu}^* = 0.79\text{--}1.18$ ) (Fig. 5a). Three samples have much higher LREE concentrations ( $\text{La}_{\text{N}} > 700$ ) (Fig. 5a). Primitive mantle-normalised trace-element diagrams of all Yegai rocks show significant enrichments in large ion lithophile elements (LILEs; e.g., Sr and Ba) and depleted high field strength element

signatures (HFSE; e.g., Nb, Ta and Ti). (Fig. 5). All Yegai samples are characterised by high Sr (up to 3636 ppm) and  $\text{Al}_2\text{O}_3$  (14.0–20.6 wt%) and depleted heavy rare earth element (HREE) signatures (Figs. 4 and 5) with high Sr/Y (29–209) ratios.

#### 4.3. Sr-Nd-Pb-B isotopes

Sr, Nd and Pb isotope results for 19 representative samples from various suites of the Yegai in the Northern Qiangtang terrane are presented in Tables 1 and 2. Apart from one moderate-Mg sample (10QT20-1) with higher radiogenic ( $^{87}\text{Sr}/^{86}\text{Sr}$ )<sub>i</sub> (0.7095) and lower  $\varepsilon_{\text{Nd}}(\text{t})$  (−9.3), the Yegai rocks have relatively uniform compositions [ $\varepsilon_{\text{Nd}}(\text{t})$  (−4.9 to −3.9) and ( $^{87}\text{Sr}/^{86}\text{Sr}$ )<sub>i</sub> (0.7070 to 0.7073)] (Fig. 6a). In terms of their Pb isotopes the Yegai samples have high ( $^{207}\text{Pb}/^{204}\text{Pb}$ )<sub>i</sub> (15.65–15.71) and ( $^{208}\text{Pb}/^{204}\text{Pb}$ )<sub>i</sub> (38.79–39.07) at a given ( $^{206}\text{Pb}/^{204}\text{Pb}$ )<sub>i</sub> (18.50–18.75) compared to the Northern Hemisphere Reference Line (NHRL; Hart, 1984) (Fig. 6c, d).

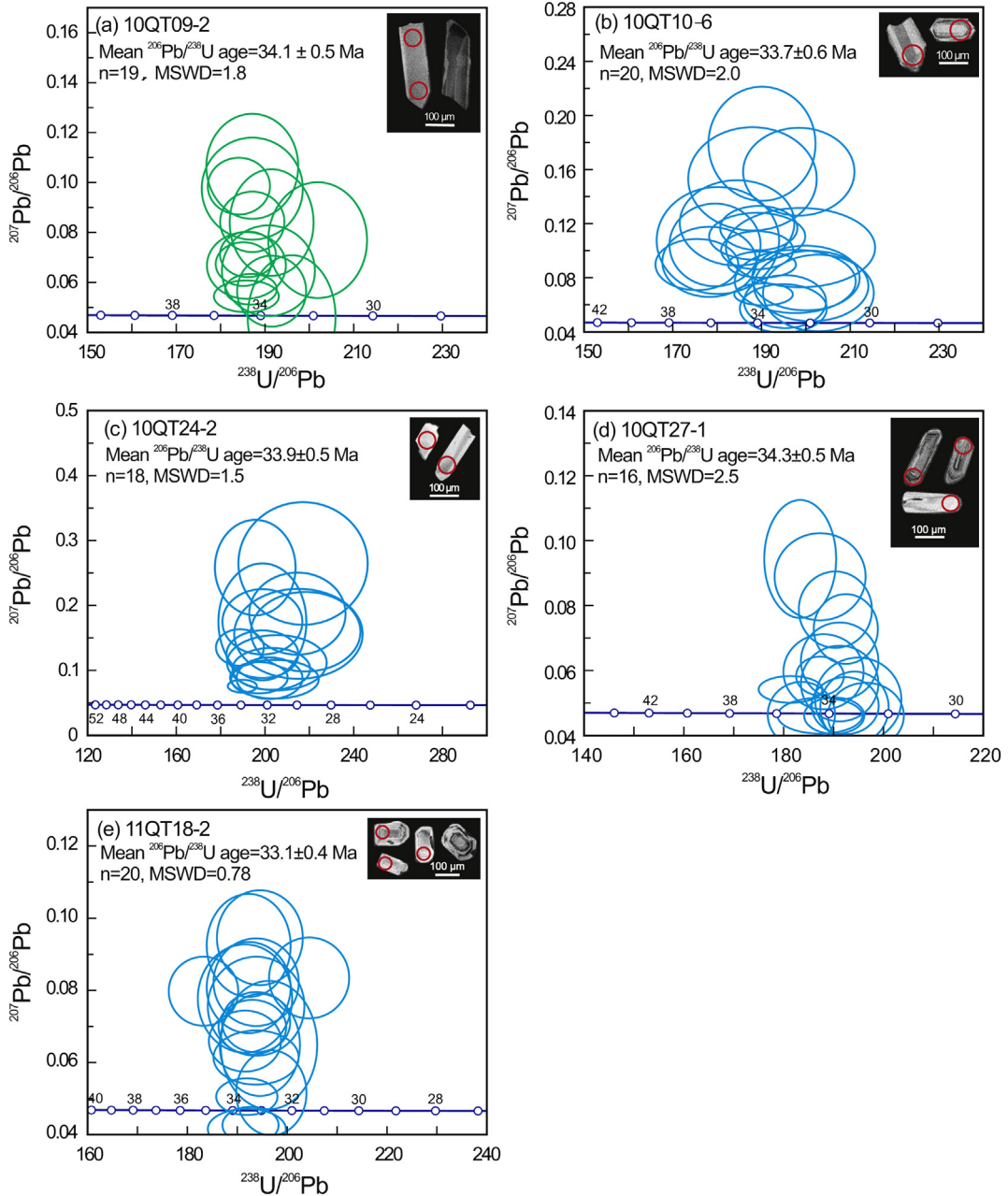


**Fig. 3.** LA-ICPMS zircon U-Pb Terra-Wasserburg (T-W) diagram diagrams with CL images for Yegai potassium-rich rock samples. (a) 10QT09-2; (b) 10QT10-6; (c) 10QT24-2; (d) 10QT27-1 and (e) 11QT18-2.

The B elemental and isotopic compositions of the Yegai rocks are given in Table 1. While their fields show some overlap, the moderate-Mg trachyandesite suite extends to lower B values (4.3–31.9 ppm) than the low-Mg trachyandesite suite (15.8–31.8 ppm) (Fig. 7c). In terms of Nb/B ratios the Yegai samples range between 0.37 and 2.91 (Fig. 7c), these values are significantly lower than the Nb/B range observed in intraplate lavas (13.0–19.1) (Ryan et al., 1996; Turner et al., 2007).

The Yegai K-rich rocks are characterised by variable and light  $\delta^{11}\text{B}$  (−20.1‰ to −7.9‰) and there is no correlation between their  $\delta^{11}\text{B}$  values and B contents. Ten of the thirteen analysed samples have  $\delta^{11}\text{B} < -10\text{\textperthousand}$ , lower than arc magmatic rocks (−9‰ to +16‰) (De Hoog and Savov, 2018; Leeman et al., 2017), altered oceanic crust (3.4 ± 1.1‰; Smith et al., 1995) and marine sediments (> −10‰, De Hoog and Savov, 2018; Tonarini et al., 2011). Four of our samples

show extremely low  $\delta^{11}\text{B}$  ranging between −20.1‰ and −18.4‰ (Fig. 7).

## 5. Discussion

### 5.1. Effects of crustal assimilation on B isotopes

Crustal assimilation along with weathering would significantly modify mantle-derived B elemental and isotopic compositions (Chaussidon and Jambon, 1994; Genske et al., 2014) and so fresh samples without weathered surfaces were selected for analyses to avoid the impact of weathering.

Continental crust has low  $\delta^{11}\text{B}$  values of ~ −16‰ to 0‰ with an average of −10‰ (Marschall and Foster, 2018). However, most of Yegai trachyte samples have lower  $\delta^{11}\text{B}$  values (down to −20.12‰) than

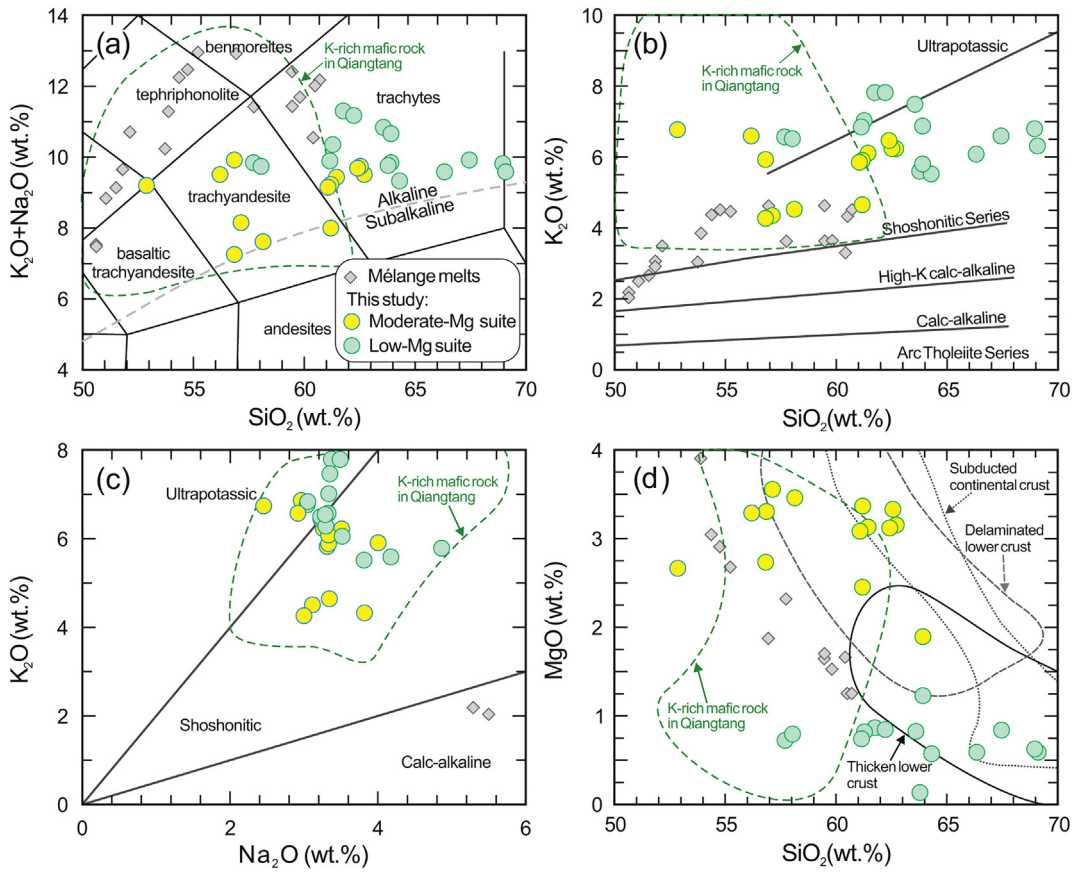


**Fig. 4.** Correlation plots of major oxides. (a)  $\text{SiO}_2$  versus  $\text{K}_2\text{O} + \text{Na}_2\text{O}$ , (b)  $\text{SiO}_2$  versus  $\text{K}_2\text{O}$ , (c)  $\text{Na}_2\text{O}$  versus  $\text{K}_2\text{O}$ , and (d)  $\text{SiO}_2$  versus  $\text{MgO}$ . Data for Cenozoic K-rich mafic rock of the Qiangtang are provided for comparison and are from Ding et al. (2003), Guo et al. (2006) and Ou et al. (2019). Mélange melts are from Cruz-Uribe et al. (2018). Fields for adakitic rocks derived from thickened lower crust, delaminated lower crust and subducted continental crust are after Wang et al. (2008).

that of sediment-derived S-type granite ( $\delta^{11}\text{B} = -11 \pm 4\text{\textperthousand}$ ) (Trumbull and Slack, 2018) and Himalayan leucogranite ( $\delta^{11}\text{B} = -15.80\text{\textperthousand}$  to  $-13.25\text{\textperthousand}$ ) (Fan et al., 2021). Thus, crustal assimilation is unlikely to be responsible for the extremely light B isotope signatures in the Yegai potassic samples. In addition, several other geochemical features also suggest insignificant crustal assimilation: a) the Yegai volcanic rocks have much lower  $[\text{Nb}/\text{La}]_{\text{PM}}$  (0.22 to 0.07) ratios than the mean value of both lower and upper continental crust ( $[\text{Nb}/\text{La}]_{\text{PM}} = 0.6$  and 0.37, respectively) (Rudnick and Gao, 2014); b) the  $(^{144}\text{Nd}/^{143}\text{Nd})_i$ ,  $(^{87}\text{Sr}/^{86}\text{Sr})_i$ , and  $(\text{Nb}/\text{La})_{\text{PM}}$  values of the Yegai samples show no significant changes with increasing  $\text{SiO}_2$  contents which might be expected if significant crustal contamination had occurred during fractionation (Fig. S1). Therefore, the variable and enriched light B isotope signatures of the Yegai samples appear to be mostly controlled by magmatic processes or source components and not by crustal contamination or post-magmatic elemental mobility.

## 5.2. Mélange origin of the Yegai potassic volcanic rocks

The petrogenesis of potassic rocks are highly controversial due to variety of proposed processes and sources, such as (1) heating and partial melting of subcontinental lithospheric mantle by rising asthenospheric mantle (Ou et al., 2019), (2) partial melting of pyroxenite in the mantle wedge (Guo et al., 2015), (3) metasomatism of harzburgite by partial melts of glimmerite (Förster et al., 2017), (4) partial melting of phlogopite-harzburgite (Condamine et al., 2016), (5) partial melting of phlogopite-free mixtures of phyllite and dunite (Wang et al., 2017), and/or (6) high-degree, fluid-absent melting of continental crust at high-T and high-P and at the expense of biotite and phengite (Campbell et al., 2014).

In this study, the two groups of Yegai samples have overlapping Sr-Nd-Pb-B isotope signatures (Figs. 6, 7) and trace element (Fig. 5) compositions and ages ( $33.8 \pm 0.4$  Ma; Fig. 3), indicating that they were derived from a common source. However, the Yegai K-rich rocks show complex compositions with low Nb/La ratios and unradiogenic Nd ( $\varepsilon_{\text{Nd}}(t) = -9.3$  to  $-3.9$ ) that preclude significant involvement of convecting asthenosphere, but rather suggest a potential contribution of continental crust. However, variable but relatively high Cr (up to 118 ppm) and Ni (up to 284 ppm) contents of the low-Mg suite samples suggest involvement of lithospheric mantle peridotite, which is distinct from the single pure crustal source as proposed by Campbell et al. (2014) (Fig. 4d). We therefore propose that the Yegai potassic rocks are derived from a hybrid source composed of mantle wedge peridotite and subducted continental crust fragment.

This hybrid model appears to be a viable model because the moderate-Mg suite has  $>3$  wt%  $\text{MgO}$  and up to 155 ppm Cr and Ni contents up to 285 ppm (Table S2). These features are broadly similar to magnesian andesites that have been derived from interaction between subducted sediment/slab melts and mantle (Tatsumi, 2006) and so mantle wedge peridotite is most likely to be one of the end-member components in formation of the Yegai K-rich rocks. On another hand, as can be seen on Fig. 7, mantle, oceanic crust (both altered and fresh) and marine sediment have  $\delta^{11}\text{B}$  values that are too high to explain the  $^{11}\text{B}$ -depleted isotope composition ( $\delta^{11}\text{B} = -20.12$  to  $-7.95\text{\textperthousand}$ ) of the Yegai K-rich samples (De Hoog and Savov, 2018). Thus, a  $^{10}\text{B}$ -rich end-member component is required. Generally, during chemical weathering, fluid mobile  $^{11}\text{B}$  is dissolved and transported to the oceans via rivers and/or groundwater, while relatively insoluble  $^{10}\text{B}$  remains in the continental regolith (Muttik et al., 2011). These residual materials (mica and clay) would have lower  $\delta^{11}\text{B}$  values (up to 20 units) than

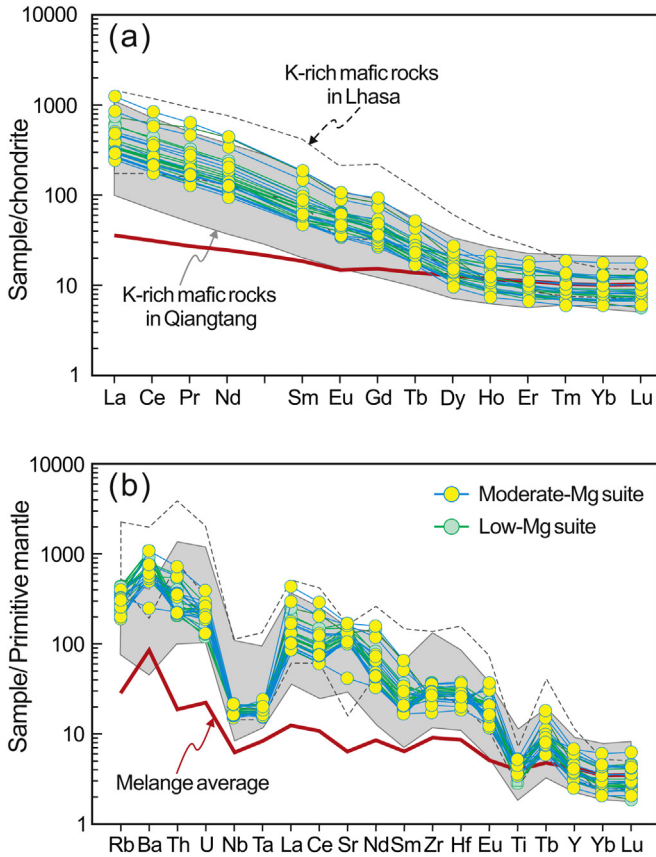


**Fig. 5.** Normalised trace element diagrams. (a) Chondrite-normalised REE and (b) primitive mantle-normalised multi-element diagrams for the Yegai potassic rocks. Data sources: Cenozoic K-rich mafic rocks in Qiangtang are from Ding et al. (2003) and Chung et al. (2005); mélange average composition is Marschall and Schumacher (2012). The data of the K-rich mafic rocks in Lhasa are from Guo et al. (2015). The chondrite and primitive mantle normalization values are from Sun and McDonough (1989).

the fresh protoliths and bulk continental crust (Romer et al., 2014; Rose et al., 2000). Previous studies also indicate that the phengite from exhumed ultrahigh-pressure (UHP) rocks in continental subduction zones has low  $\delta^{11}\text{B}$  values of  $-29\text{\textperthousand}$ . (Menold et al., 2016). Thus, sediment-bearing continental crust may be another important end-

member component. The Sr-Nd isotope modelling further suggest that a contribution of sediment may be responsible for the high Nd/Sr ratio in some samples (Fig. 8b).

Here we further propose a mélange source to explain origin and compositional features of the Yegai K-rich rocks. Mélange rocks, are formed by mechanical mixing, metasomatic interactions and diffusion at different P-T conditions (Bebout and Penniston-Dorland, 2016; Guillot et al., 2009) and proposed as a magmatic source in the oceanic subduction zones (Marschall and Schumacher, 2012; Nielsen and Marschall, 2017). The mélange model is also used to explain the formation of post-collisional potassic rocks in Tibet (Guo et al., 2013, 2014, 2015). The continental crust fragments with sediments were likely sheared downward by subducting crust to 80 km depths where devolatilization took place (Menold et al., 2016; Schmidt and Poli, 1998) to form a mélange source for the Yegai potassic rocks (Fig. 9). The subcontinental lithospheric mantle is usually refractory at the low geothermal gradients of subduction zones (Zheng, 2012), whereas sediments have relatively low solidus temperatures at high pressure ( $775 \pm 25^\circ\text{C}$  at 2 GPa) (Johnson and Plank, 2000). Dehydration melting of phengite-bearing eclogite occurs at 1.5–2.0 GPa and  $800\text{--}850^\circ\text{C}$  (Liu et al., 2019). Thus, a sediment-bearing mélange source would be more conducive to melting compared with a pure continental lithospheric mantle. The high Sr and low Yb contents of the Yegai potassic rocks and the reported coeval (ca. 42–38 Ma) adakitic rocks in north Qiangtang (e.g., Long et al., 2015; Ou et al., 2017), suggest a plagioclase-free and garnet-bearing source, deeper than 50 km. The zircon saturation thermometer by Boehnke et al. (2013) also yields moderate temperatures ( $T_{\text{Zr}}$ ) ( $663\text{--}899^\circ\text{C}$ ) for Yegai K-rich rocks. In addition, uniform Nd isotopic compositions with variable Nd/Hf ratios for Yegai samples are also one main feature of mélange source (Nielsen and Marschall, 2017) (Fig. 8). All these suggest that partial melting of mélange within continental subduction channel is most likely to form the small-volume Yegai K-rich rocks in continental collision orogen, similar to the Anatolian of Turkey example (e.g., Palmer et al., 2019).

Fractional crystallisation or crustal contamination are the common explanations for magmas with relatively high  $\text{SiO}_2$  and low  $\text{MgO}$  compositions. However, with the exception of  $\text{CaO}$ , lack of correlation between  $\text{MgO}$  and other major element oxides precludes the possibility that the low-Mg suite were derived by fractional crystallisation from the moderate-Mg suite (Fig. S2). In addition, overlapping Cr and Ni contents and weak Eu anomalies ( $\text{Eu}^*/\text{Eu} = 0.8\text{--}1.1$ ) for moderate- and low-Mg suites also do not support significant fractional crystallisation of clinopyroxene and plagioclase (Fig. 5 and Fig. S2). The variation of Cr-Ni contents of each suite is thus more likely to be derived from the

**Table 1**  
Bulk-rock Sr-Nd-B isotopic data for the Yegai igneous rocks.

Sample	Rb (ppm)	Sr (ppm)	$^{87}\text{Sr}/^{86}\text{Sr} \pm 2\sigma$	$(^{87}\text{Sr}/^{86}\text{Sr})_i$	Sm (ppm)	Nd (ppm)	$^{143}\text{Nd}/^{144}\text{Nd} \pm 2\sigma$	$(^{143}\text{Nd}/^{144}\text{Nd})_i$	$\varepsilon_{\text{Nd}}(t)$	$\delta^{11}\text{B}$ (‰)	$2\sigma$	B (ppm)
10QT09-2	227.2	2397	$0.707177 \pm 5$	0.707049	11.67	72.81	$0.512408 \pm 4$	0.512387	-4.08	-13.40	0.03	15.8
10QT09-3	216.7	2383	$0.707149 \pm 5$	0.707026	10.77	68.27	$0.512402 \pm 6$	0.512381	-4.19			
10QT09-4	245.8	2767	$0.707198 \pm 6$	0.707078	10.76	65.86	$0.512411 \pm 4$	0.512389	-4.02			
10QT09-5	276.7	2939	$0.707175 \pm 6$	0.707048	11.93	77.05	$0.512403 \pm 4$	0.512382	-4.16			
10QT09-6	280.4	3198	$0.707165 \pm 6$	0.707041	12.46	80.69	$0.512408 \pm 4$	0.512388	-4.05	-11.14	0.03	18.9
10QT10-1	378.2	1888	$0.70749 \pm 5$	0.707218	7.187	39.81	$0.512404 \pm 5$	0.51238	-4.2			
10QT10-4	231.9	2489	$0.707377 \pm 6$	0.707251	9.612	66.22	$0.512397 \pm 4$	0.512377	-4.25	-18.41	0.03	26.5
10QT20-3	172.9	3568	$0.707374 \pm 6$	0.707308	14.8	104.2	$0.512389 \pm 3$	0.51237	-4.4	-9.97	0.03	31.9
10QT10-6	206	2242	$0.707175 \pm 7$	0.70705	9.382	59.4	$0.512403 \pm 4$	0.512382	-4.17			
10QT10-7	209.7	2165	$0.707151 \pm 6$	0.707019	9.203	59.23	$0.512417 \pm 4$	0.512397	-3.88			
10QT10-9	230.2	2170	$0.70727 \pm 5$	0.707127	7.831	52.98	$0.512397 \pm 5$	0.512377	-4.26	-12.99	0.03	31.9
10QT20-1	208	880.1	$0.709817 \pm 7$	0.709497	7.206	43.94	$0.512140 \pm 4$	0.512118	-9.31	-20.12	0.03	18.7
10QT24-2	124.1	2702	$0.707000 \pm 5$	0.706938	15.18	106.7	$0.512387 \pm 4$	0.512369	-4.43	-9.52	0.03	5.72
10QT26-1	141.9	2797	$0.707001 \pm 5$	0.706932	9.073	66.11	$0.512385 \pm 5$	0.512367	-4.46	-14.42	0.03	7.45
10QT26-2	134.3	2767	$0.707035 \pm 5$	0.706969	12.52	88.57	$0.512388 \pm 3$	0.512369	-4.42	-18.45	0.03	4.29
10QT27-1	247.9	2357	$0.707112 \pm 6$	0.70697	7.357	46.87	$0.512406 \pm 5$	0.512386	-4.09	-8.13	0.03	23.6
11QT18-1	196.1	3636	$0.707216 \pm 7$	0.707143	29.14	212.6	$0.512368 \pm 4$	0.51235	-4.79	-15.61	0.04	16.3
11QT18-2	166.4	3459	$0.707196 \pm 7$	0.707131	22.98	162.1	$0.512363 \pm 4$	0.512345	-4.89	-7.95	0.03	18.4
11QT21-2	158	2879	$0.707193 \pm 5$	0.707118	28.47	201.4	$0.512385 \pm 3$	0.512367	-4.47	-14.55	0.05	6.83

**Table 2**

Bulk-rock Pb isotopic data for the Yegai igneous rocks.

Sample	Pb (ppm)	U (ppm)	Th (ppm)	$^{206}\text{Pb}/^{204}\text{Pb}$	2σ	$^{207}\text{Pb}/^{204}\text{Pb}$	2σ	$^{208}\text{Pb}/^{204}\text{Pb}$	2σ	$(^{206}\text{Pb}/^{204}\text{Pb})_i$	$(^{207}\text{Pb}/^{204}\text{Pb})_i$	$(^{208}\text{Pb}/^{204}\text{Pb})_i$
10QT09-2	579.3	2.584	19.08	18.6357	0.0003	15.6765	0.0003	38.9483	0.0012	18.63	15.68	38.94
10QT09-3	630.6	3.212	18.89	18.6355	0.0003	15.6760	0.0003	38.9473	0.0012	18.63	15.68	38.94
10QT09-4	919.2	4.171	18.24	18.6369	0.0003	15.6766	0.0002	38.9497	0.0009	18.64	15.68	38.95
10QT09-5	526.7	4.309	22.09	18.6351	0.0003	15.6770	0.0003	38.9467	0.0011	18.63	15.68	38.94
10QT09-6	400.3	4.325	23.54	18.6357	0.0003	15.6760	0.0003	38.9464	0.0011	18.63	15.68	38.94
10QT10-1	59.76	4.489	22.27	18.6536	0.0003	15.6754	0.0003	38.9654	0.0010	18.63	15.67	38.93
10QT10-4	73.87	5.104	24.92	18.6526	0.0003	15.6741	0.0003	38.9570	0.0010	18.63	15.67	38.92
10QT20-3	57.28	5.838	50.64	18.7188	0.0003	15.6895	0.0003	39.0900	0.0010	18.69	15.69	39.00
10QT10-6	139.7	3.976	18.85	18.6323	0.0003	15.6741	0.0002	38.9367	0.0009	18.62	15.67	38.92
10QT10-7	127.9	4.108	18.73	18.6324	0.0003	15.6727	0.0003	38.9310	0.0012	18.62	15.67	38.92
10QT10-9	46.36	5.281	20.79	18.6585	0.0003	15.6748	0.0003	38.9656	0.0010	18.62	15.67	38.92
10QT20-1	152.5	2.765	18.94	18.6708	0.0003	15.6701	0.0003	38.9548	0.0009	18.66	15.67	38.94
10QT24-2	38.69	6.317	31.12	18.7723	0.0003	15.6874	0.0003	39.1602	0.0010	18.72	15.68	39.07
10QT26-1	40.83	4.137	28.85	18.7502	0.0003	15.6857	0.0003	39.1327	0.0011	18.72	15.68	39.06
10QT26-2	41.42	4.654	31.12	18.7546	0.0003	15.6854	0.0002	39.1422	0.0011	18.72	15.68	39.06
10QT27-1	61.53	5.725	18.3	18.5330	0.0003	15.6556	0.0003	38.8228	0.0010	18.50	15.65	38.79
11QT18-1	9.058	8.393	61.36	19.0382	0.0003	15.7181	0.0003	39.6539	0.0009	18.74	15.70	38.93
11QT18-2	19.28	4.225	48.24	18.8249	0.0003	15.7111	0.0003	39.2991	0.0009	18.75	15.71	39.03
11QT21-2	35.96	4.238	35.34	18.7660	0.0004	15.6984	0.0004	39.1343	0.0011	18.73	15.70	39.03

proportion and degree of molten differences of each component in the source.

Numerous experiments and studies indicate that melt compositions may be controlled by  $\text{H}_2\text{O}$  and  $\text{CO}_2$  contents (Liu et al., 2006; Mitchell and Grove, 2015). Liu et al. (2006) showed that each percent addition of  $\text{H}_2\text{O}$  to source would result in a 0.6% increase in  $\text{SiO}_2$  content and about 1.3% decrease in  $\text{MgO}$  of melt (on an anhydrous basis). As mentioned above, the suites of Yegai K-rich samples are more likely derived from a similar source but with variable volatile and olivine components. The features of the low-Mg suite likely result from the potential high volatile ( $\text{H}_2\text{O}$  and  $\text{CO}_2$ ) components in the source, which may be inherited from the pre-collision lithospheric mantle source during oceanic subduction (Goussin et al., 2020; Ma et al., 2021). In addition, the

LREE signature of sediment melts in subduction zones are considered to be controlled by the solubility of accessory mineral phases, such as monazite and allanite (Hermann and Rubatto, 2009). The solubility of monazite has a strong temperature and pressure dependence (Stepanov et al., 2012). Simplified modelling also indicates that a 0.1% increase in solubility of monazite could be responsible for features of the Yegai high-LREE samples (Fig. S3).

### 5.3. Light boron isotope fractionation and cycling in continental collision system

Boron is very soluble and enriched in continental crust by several orders of magnitude relative to B-poor mantle (e.g., Marschall et al., 2007;

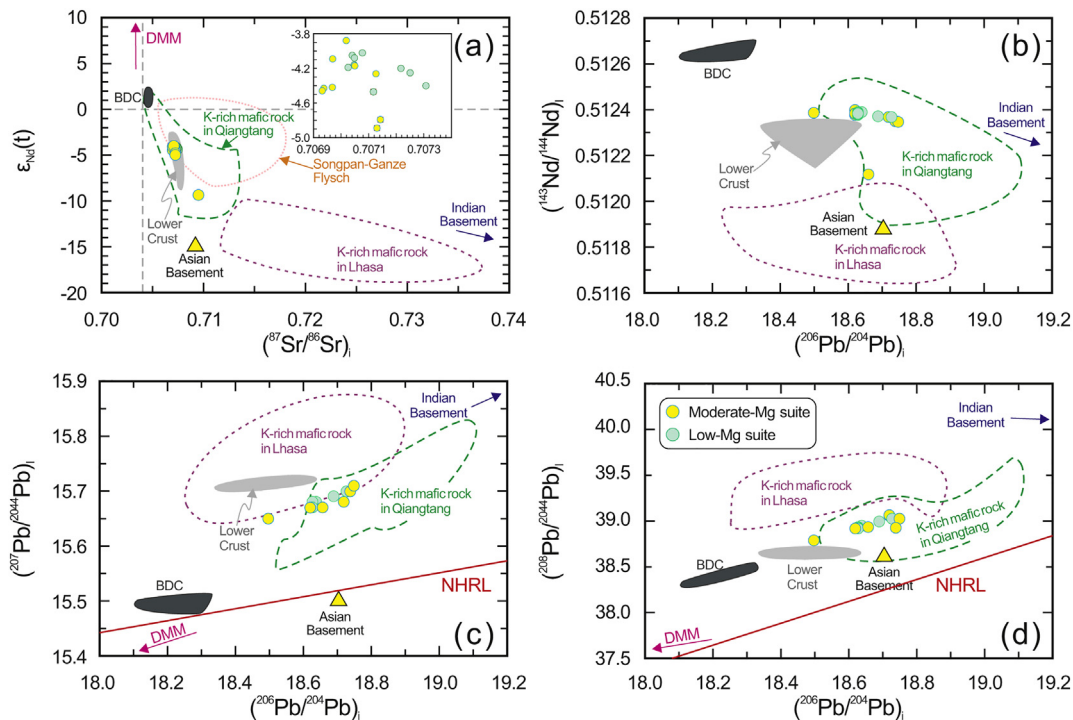


**Fig. 6.** Sr-Nd-Pb isotope systematics. Plots of (a)  $\epsilon_{\text{Nd}}$  (34 Ma) vs  $(^{87}\text{Sr}/^{86}\text{Sr})_i$ , (b)  $(^{142}\text{Nd}/^{144}\text{Nd})_i$  vs  $(^{206}\text{Pb}/^{204}\text{Pb})_i$ , (c)  $(^{207}\text{Pb}/^{204}\text{Pb})_i$  vs  $(^{206}\text{Pb}/^{204}\text{Pb})_i$ , (d)  $(^{208}\text{Pb}/^{204}\text{Pb})_i$  vs  $(^{206}\text{Pb}/^{204}\text{Pb})_i$ . The Sr-Nd-Pb isotope data for samples from this study are from Tables S5 and S6. Arrows point towards the composition of depleted MORB-source mantle (DMM) (Workman and Hart, 2005), Indian continental basement (Guo and Wilson, 2012) and Asian basement (Guo et al., 2014). The NHRL (Northern Hemisphere Reference Line) in (c) and (d) is from Hart (1984). The BDC (Bangdacuo) sodium basalts representing Qiangtang mantle before Eocene are from Ding et al. (2003).

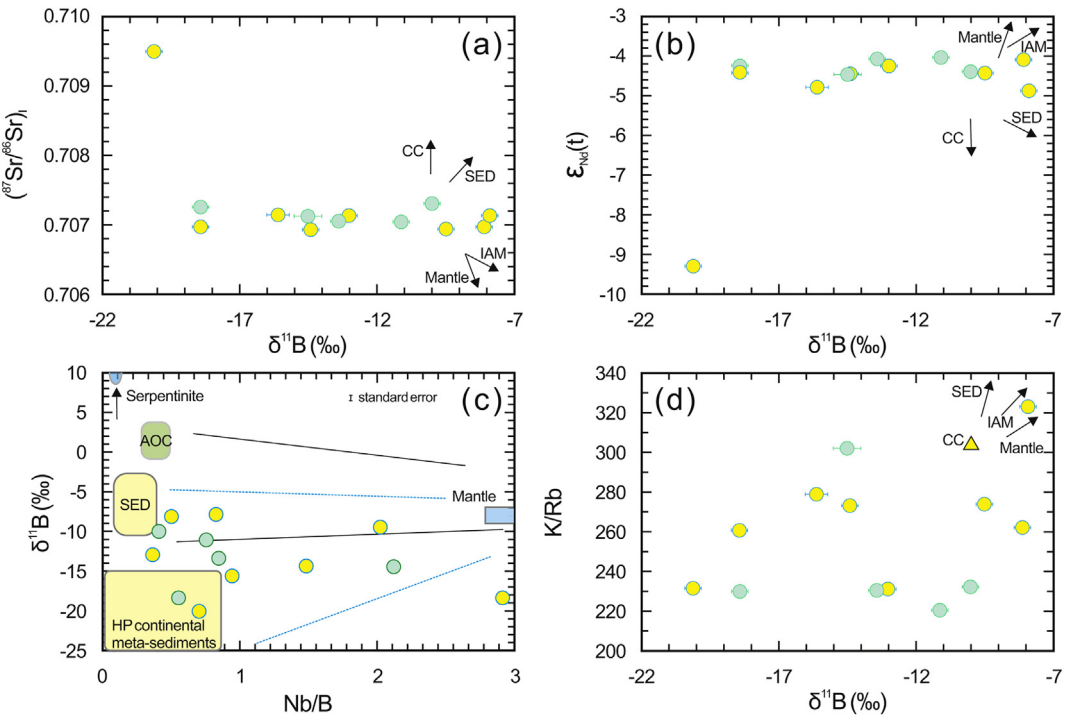


**Fig. 7.** Variation diagrams of  $\delta^{11}\text{B}$  with isotopes and element ratios. (a)  $^{87}\text{Sr}/^{86}\text{Sr}_i$  versus  $\delta^{11}\text{B}$ , (b)  $\epsilon_{\text{Nd}}(t)$  versus  $\delta^{11}\text{B}$ , (c)  $\delta^{11}\text{B}$  versus Nb/B, and (d) K/Rb diagrams for volcanic rocks from Yegai of northern Tibet. The mantle data includes OIB (Sun and McDonough, 1989; Tanaka and Nakamura, 2005) and ocean ridge basalt data (Marschall et al., 2017). Marine and high-pressure continental sediments data are from Ryan and Chauvel (2014) and Trumbull and Slack (2018). Abbreviations: AOC – altered oceanic crust; SED – (marine) sediment; IAM – island arc magma; CC – continental crust. The areas between black and blue lines represents the general ranges of magma in oceanic and continental subduction zones, respectively (Marschall et al., 2017).

Palmer, 2017). These make boron a sensitive tracer of the role of fluids in subduction zones. Studies over the past few decades have helped develop an understanding of the B isotope fractionation and cycling in oceanic subduction zones (De Hoog and Savov, 2018; Marschall et al., 2017;

Palmer, 2017; Ryan and Chauvel, 2014). In oceanic subduction zones, boron predominantly occurs in sediments that are derived from continental crust or by adsorption of clay minerals from seawater (Palmer, 2017). Prior to subduction, millions of years of interaction with

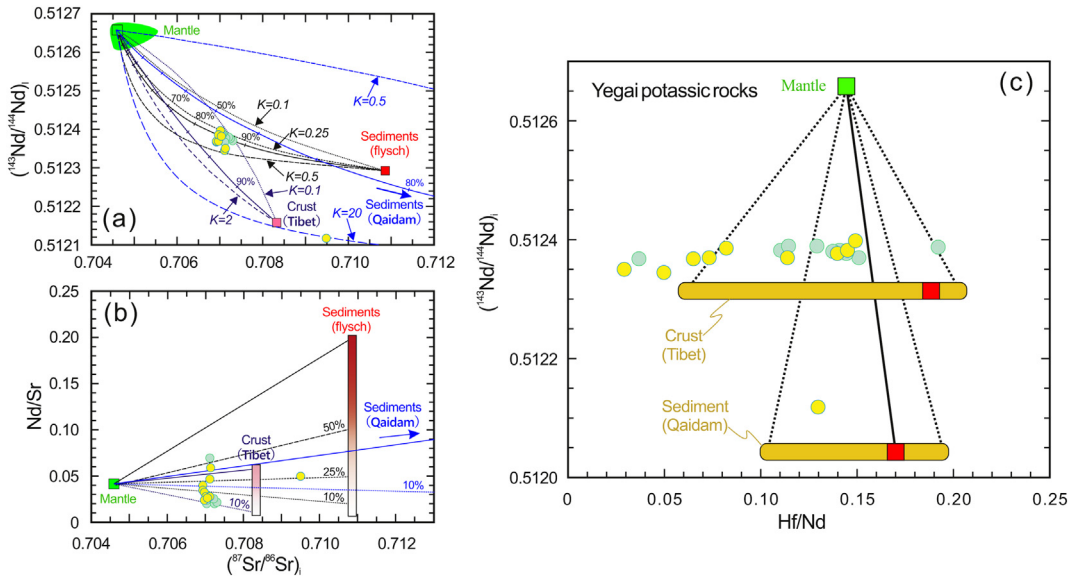


**Fig. 8.** Mixing modelling diagrams of mélange source for Yegai potassic lava of northern Tibet. Plots of  $(^{143}\text{Nd}/^{144}\text{Nd})_i$  versus  $(^{87}\text{Sr}/^{86}\text{Sr})_i$  (a), Nd/Sr versus  $(^{87}\text{Sr}/^{86}\text{Sr})_i$  (b) and  $(^{143}\text{Nd}/^{144}\text{Nd})_i$  versus Hf/Nd ratios. Data source: mantle represented by sodic basalts of northern Qiangtang ( $\text{Sr} = 1122 \text{ ppm}$ ;  $\text{Nd} = 46 \text{ ppm}$ ;  $^{87}\text{Sr}/^{86}\text{Sr}_{(i)} = 0.7046$ ;  $^{143}\text{Nd}/^{144}\text{Nd}_{(i)} = 0.5127$ ) (Ding et al., 2003); flysch sediments of Songpan-Ganze ( $\text{Sr} = 114.8 \text{ ppm}$ ;  $\text{Nd} = 22.88 \text{ ppm}$ ;  $^{87}\text{Sr}/^{86}\text{Sr}_{(i)} = 0.7109$ ;  $^{143}\text{Nd}/^{144}\text{Nd}_{(i)} = 0.5123$ ) (She et al., 2006); terrigenous sediments of Qaidam ( $\text{Sr} = 163 \text{ ppm}$ ;  $\text{Nd} = 24 \text{ ppm}$ ;  $^{87}\text{Sr}/^{86}\text{Sr}_{(i)} = 0.7232$ ;  $^{143}\text{Nd}/^{144}\text{Nd}_{(i)} = 0.5120$ ) (Chen et al., 2015); Tibetan lower crust represented by adakitic rocks of Qiangtang ( $\text{Sr} = 384 \text{ ppm}$ ;  $\text{Nd} = 22.1 \text{ ppm}$ ;  $^{87}\text{Sr}/^{86}\text{Sr}_{(i)} = 0.7083$ ;  $^{143}\text{Nd}/^{144}\text{Nd}_{(i)} = 0.5111$ ) (Long et al., 2015; Ou et al., 2017). Details of mixing: (a) The mixing curves were constructed using different Sr/Nd elemental ratios,  $K = (\text{Sr}/\text{Nd})_{\text{Mantle}}/(\text{Sr}/\text{Nd})_{\text{respective mixing components}}$ ; The percentage indicates the proportion of mantle component. (b) The percentage indicates the proportion of respective mixing components.

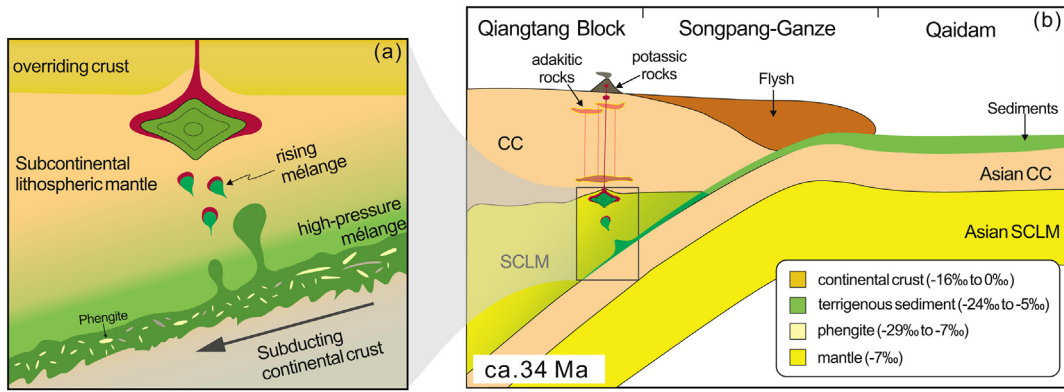


**Fig. 9.** Schematic diagram illustrating melting of mélange in an intraplate continental subduction zone. (a) Conceptual illustration of melting of mélange diapir after Cruz-Uribe et al. (2018). (b) The Asian continent plate with considerable sediments was passive thrust below the Tibetan plate before the end of Eocene.

circulating seawater result in most oceanic crust, including sediments, having isotopically heavy and B-rich geochemical signatures ( $\delta^{11}\text{B} = -5$  to  $+5\text{\textperthousand}$ ) (Palmer, 2017). Arc magmas are thus characterised by relatively heavy  $\delta^{11}\text{B}$  signatures ( $= -10$  to  $+15\text{\textperthousand}$ ) (Ryan and Chauvel, 2014) and enriched fluid active elements (Tatsumi and Eggins, 1995) due to fluid sources with more concentrated heavy isotopes, such as serpentinite (Tomanikova et al., 2019). However, a different process is required to explain the light boron isotopic features of the potassic magmas from continental collision and subduction zones (Palmer et al., 2019).

As mentioned above, mica and clay in the continental regolith is a substantial reservoir of isotopically light  $^{10}\text{B}$  component (Muttik et al., 2011; Rose et al., 2000). Generally, these components are difficult to transport deep into the Earth, because of their low density. Our data suggest the isotopically light component was subducted deeply in the Tibetan orogen, and likely formed a distinct mantle reservoir (Fig. 9). A similar model has been proposed by Palmer et al. (2019) for the Anatolian collision zone in Turkey.

Boron is a soluble element and is expected to be enriched in devolatilized fluids and depleted in the high-pressure/temperature meta-metasedimentary rocks (Bebout et al., 2007; Marschall et al., 2007). Our simplified Rayleigh fractionation modelling results also indicate that devolatilized fluids would remove the relatively solvable  $^{11}\text{B}$ , leaving relatively insoluble  $^{10}\text{B}$  that remains in the phengite of subducted continental crust. This results in further fractionation of B isotopes (Fig. 10). Approximately 40% of the dehydrated fluid fraction with parameters  $\alpha$  of 1.01 and  $D_{\text{B}}^{\text{Rock/Fluid}}$  of 0.2 could be responsible for

the B isotopic compositional characterizations of the Yegai K-rich rocks in central Tibet (Fig. 10).

Although a significant portion of the boron is carried back the shallow crust by the dehydrating fluid, the remaining isotopically lighter components would be carried deeper into the mantle to form a distinct mantle reservoir (Figs. 9, 10b). This isotopically light mantle reservoir is sampled by potassium-rich magmas and subsequently re-enters the crust, so completing the cycle of the light B isotopic component (Fig. 9). Given the limited volume of potassic magma and high partition coefficient  $D_{\text{B}}^{\text{Phengite-Clinopyroxene}}$  of 5 (Zack et al., 2002), a significant amount of isotopically light B component would still be preserved in phengite in the mantle. Our study demonstrates that the isotopically light boron component could be subducted deeply into the mantle and boron isotope have potential to trace the role of subducted continental crust and sediment in the origin of mafic K-rich rocks in continental collision systems.

#### 5.4. Implications for dynamics and continental crust recycling

Over the last 20 years, it has remained unclear, based on seismic images (e.g., Kind et al., 2002; Zhao et al., 2010; Zhao et al., 2011) and magmatic rocks (e.g., Chung et al., 2005; Turner et al., 1993; Wang et al., 2008) if the Asian continent did indeed subduct during Eocene even earlier (Tapponnier et al., 2001). The main objection to subduction of the Asian continent is that continental subduction would have terminated the magmatism in a similar manner to the 40–30 Ma cessation of magmatism in southern Tibet during subduction of Indian

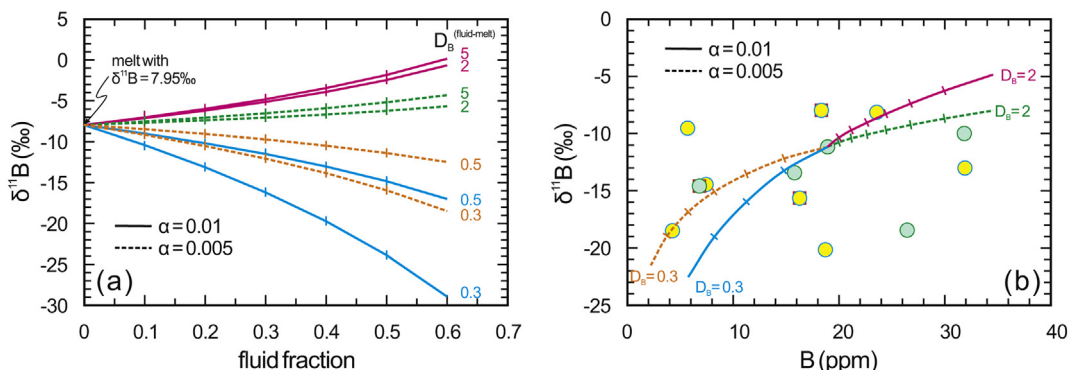


**Fig. 10.** Boron isotopic fractionation modeled by the Rayleigh dehydration model (Ishikawa et al., 2001; Kaliwoda et al., 2011). (a) Boron isotope variation with fluid fraction. Starting materials are sample 11QT18-2 with  $\delta^{11}\text{B} = -7.95\text{\textperthousand}$ . Parameters used are  $\alpha = 1.01$  (solid lines) and  $\alpha = 1.005$  (dotted lines). The bulk B distribution coefficients are  $D_{\text{B}} = 2-5$  for the melt residues (red and green lines), and  $D_{\text{B}} = 0.3-0.5$  for the solid residues (blue and orange lines) after fluid extraction, respectively. (b) Results of B element and isotope modelling. Starting materials are sample 10QT09-6 with  $\delta^{11}\text{B} = -11.14\text{\textperthousand}$  and  $B = 18.93 \text{ ppm}$ .

lithosphere (Chung et al., 2005). Therefore, lithospheric mantle thinning and/or delamination has been proposed as an alternative mechanism for both uplift of plateau and the generation of Eocene-Oligocene small-volume mafic potassic rocks, widespread in northern Qiangtang (Chung et al., 1998; Turner et al., 1993). However, these mafic potassic rocks are distributed in a near-linear trend along the Jinsha suture (Fig. 1), a feature inconsistent with magmatic distribution during lithospheric mantle thinning and/or delamination. Moreover, low Nb/La ratios and unradiogenic Nd ( $\varepsilon_{\text{Nd}} = -9.3$  to  $-3.9$ ) also do not support involvement of upwelling asthenosphere which is expected as a result of delamination. In the lithospheric delamination model, an inherited enriched lithospheric mantle is required. However, recent studies on Late Mesozoic sodic volcanic rocks reveal that there was a pre-collisional carbonated lithosphere with depleted characteristics beneath the northern Qiangtang (Ma et al., 2021). This implies that an extra process is required to explain the enrichment of the Qiangtang lithosphere during Cenozoic.

The light boron isotope characteristics, similar to high-pressure phengite, provide clear evidence for recycling of continental crust, as proposed from other collisional orogenic systems (Hermann et al., 2013; Palmer et al., 2019; Zheng, 2012). Moreover, the emplacement of these Eocene to Oligocene magmas is associated with thrust faults and an east–west trending *syn*-contractional basin (Chung et al., 2005; Kapp et al., 2005; Spurlin et al., 2005), which probably are a response to north-south convergence between the Indian and Asian continents (Li et al., 2015; Wang et al., 2002). Accordingly, our new B isotope data, combined with geophysical data (Zhao et al., 2010; Zhao et al., 2011), indicates that the Asian plate was likely overridden by the Tibetan plate before the end of Eocene (Fig. 6). The position of Asian continent has not moved significantly since the Cenozoic (Cogné et al., 2013), so the reason for subduction of the Asian continent is more likely to be because the Tibetan plate has been thrust upward over the margin of Asian continent. This occurred along the Jin-Sha and Anymaqen-Kunlun-Muztagh ancient sutures due to the strong northward convergence of the Indian continent (Ou et al., 2019; Wang et al., 2008). With the thickening of the overlying Tibetan plate during obduction, eclogite forms at the leading edge of the subducting continental slab, this increase in density can pull the slab further into the mantle.

The eclogitic metamorphism may occur in the front of the Asian continent and provide the traction force for continental subduction. These hypotheses need to be tested in the future.

A long-standing problem in the geological evolution of the India-Asia collision zone is how and where convergence between India and Asia was accommodated since collision (van Hinsbergen et al., 2011). A greater India has been proposed to accommodate ~2400–3200 km of India-Asia convergence by subduction or underthrusting (e.g., van Hinsbergen et al., 2011). Given that approximately half of the present India-Asia convergence is accommodated north of  $32^{\circ}\text{N}$  (Zhang et al., 2004), we suggest that this potential Asian continent subduction could play a significant role in accommodating the convergence in central and northern Tibet. In addition, such a simultaneous double subduction of the Indian and Asian continents could help explain India's rapid movement towards Eurasia during Eocene i.e., after continental collision (convergence rate between the Indian and Asian continents of 70–90 mm/yr, van Hinsbergen et al., 2011).

Mass balance calculations suggest as much as half of the pre-collisional Indian continental crust was lost during Indo-Asian collision (Ingalls et al., 2016). Although it is generally believed that only the eclogitized lower crust can subduct into the mantle, the markedly light boron isotope composition of mantle-derived potassic rocks from collisional belts (Palmer et al., 2019 and this study) provide clear evidence for deep subduction of the continental crust with sediments. Such continental crust recycling is unlikely to be unique to the Tethyan tectonic belt and has probably also occurred during previous large-scale collisional orogenic events, such as the Variscan of central Europe, the Pan-African, and the Grenville as proposed by Ingalls et al. (2016).

Consequently, such continental crust subduction is likely to have had a significant impact on the compositional evolution of the continental crust and mantle throughout much of Earth history.

## 6. Conclusions

- 1) Eocene-Oligocene Yegai potassium-rich rocks in northern Qiangtang are characterised by adakite-like trace elements, enriched Sr-Nd-Pb and light B isotope signatures.
- 2) These K-rich rocks were most likely derived from a mélange source composed of mantle wedge peridotite and continental crust fragments.
- 3) Dehydration of subducted continental crust with sediments may cause fractionation of boron isotopes in continental subduction zones.
- 4) The isotopically light  $^{10}\text{B}$  component is deeply subducted in collisional orogens, and may form a distinct mantle reservoir that was sampled by potassium-rich magmas.
- 5) The Tibetan plate may have overridden the Asian plate before the end of Eocene.

## Declaration of Competing Interest

The authors declare that they have no known competing financial interests or personal relationships that could have appeared to influence the work reported in this paper.

## Acknowledgments

We thank editor in chief Prof. Xian-Hua Li and two anonymous reviewers for their constructive suggestions and comments that helped us improve the paper substantially. We appreciate the assistance of Ying Liu, Yue-Heng Yang, Xi-Rong Liang, Jin-Long Ma, Guang-Qian Hu, Xiang-Lin Tu and Le Zhang for zircon age and whole rock geochemical analyses. We also thank Dr. Wei Dan for his valuable suggestions. Financial support for this research was provided by the National Natural Science Foundation of China (Nos. 41630208, 91855215, and 41872062), the Second Tibetan Plateau Scientific Expedition and Research (STEP) (2019QZKK0702), the Strategic Priority Research Program (A) of the Chinese Academy of Sciences (No. XDA2007030402), the National Key Research and Development Project of China (2016YFC0600309) and the Youth Innovation Promotion Association CAS (2017404). This is contribution No. IS-3006 from GIGCAS. Analysis methods and the data supporting these conclusions can be found in supporting information Text S1, Figs. S1–S6 and Tables S1–S6 and EarthChem Library (DOI: [10.26022/IEDA/111630](https://doi.org/10.26022/IEDA/111630), Geochemistry data of the Yegai magmatic rocks in northern Tibet, <http://www.earthchem.org/library>).

## Appendix A. Supplementary data

Supplementary data to this article can be found online at <https://doi.org/10.1016/j.lithos.2021.106146>.

## References

- Bebout, G.E., Penniston-Dorland, S.C., 2016. Fluid and mass transfer at subduction interfaces—the field metamorphic record. *Lithos* 240, 228–258.
- Bebout, G.E., Bebout, A.E., Graham, C.M., 2007. Cycling of B, Li, and LILE (K, Cs, Rb, Ba, Sr) into subduction zones: SIMS evidence from micas in high-P/T metasedimentary rocks. *Chem. Geol.* 239, 284–304.
- Boehnke, P., Watson, E.B., Trail, D., Harrison, T.M., Schmitt, A.K., 2013. Zircon saturation revisited. *Chem. Geol.* 351, 324–334.
- Campbell, I.H., Stepanov, A.S., Liang, H.-Y., Allen, C.M., Norman, M.D., Zhang, Y.-Q., Xie, Y.-W., 2014. The origin of shoshonites: new insights from the Tertiary high-potassium intrusions of eastern Tibet. *Contrib. Mineral. Petro.* 167, 983 (2014). <https://doi.org/10.1007/s00410-00014-00983-00419>.
- Chaussidon, M., Jambon, A., 1994. Boron content and isotopic composition of oceanic basalts: geochemical and cosmochemical implications. *Earth Planet. Sci. Lett.* 121, 277–291.

- Chen, X., Gehrels, G., Yin, A., Zhou, Q., Huang, P., 2015. Geochemical and Nd-Sr-Pb-O isotopic constrains on Permo-Triassic magmatism in eastern Qaidam Basin, northern Qinghai-Tibetan plateau: implications for the evolution of the Paleo-Tethys. *J. Asian Earth Sci.* 114, 674–692.
- Chen, M., Niu, F., Tromp, J., Lenardic, A., Lee, C.-T.A., Cao, W., Ribeiro, J., 2017. Lithospheric foundering and underthrusting imaged beneath Tibet. *Nat. Commun.* 8, 15659 (12017). (<https://doi.org/10.11038/ncomms15659>).
- Chung, S.-L., Lo, C.-H., Lee, T.-Y., Zhang, Y., Xie, Y., Li, X., Wang, K.-L., Wang, P.-L., 1998. Diachronous uplift of the Tibetan plateau starting 40 Myr ago. *Nature* 394, 769–773.
- Chung, S.L., Chu, M.F., Zhang, Y., Xie, Y., Lo, C.H., Lee, T.Y., Lan, C.Y., Li, X., Zhang, Q., Wang, Y., 2005. Tibetan tectonic evolution inferred from spatial and temporal variations in post-collisional magmatism. *Earth Sci. Rev.* 68, 173–196.
- Cogné, J.-P., Besse, J., Chen, Y., Hankard, F., 2013. A new late cretaceous to present APWP for Asia and its implications for paleomagnetic shallow inclinations in Central Asia and Cenozoic Eurasian plate deformation. *Geophys. J. Int.* 192, 1000–1024.
- Collins, W.J., Belousova, E.A., Kemp, A.I.S., Murphy, J.B., 2011. Two contrasting Phanerozoic orogenic systems revealed by hafnium isotope data. *Nat. Geosci.* 4, 333–337.
- Condamine, P., Médard, E., Devidal, J.-L., 2016. Experimental melting of phlogopite-peridotite in the garnet stability field. *Contrib. Mineral. Petro.* 171, 1–26.
- Cruz-Uribe, A.M., Marschall, H.R., Gaetani, G.A., Le Roux, V., 2018. Generation of alkaline magmas in subduction zones by partial melting of mélange diapirs—an experimental study. *Geology* 46, 343–346.
- De Hoog, J.C., Savov, I.P., 2018. Boron isotopes as a tracer of subduction zone processes. *Boron Isotopes*. Springer, pp. 217–247.
- Deng, W., 1998. Cenozoic intraplate volcanic rocks in the northern Qinghai-Xizang plateau. In: Geological Publishing House pp. 180.
- Ding, L., Kapp, P., Zhong, D., Deng, W., 2003. Cenozoic volcanism in Tibet: evidence for a transition from oceanic to continental subduction. *J. Petrol.* 44, 1833–1865.
- Dupont-Nivet, G., Krijgsman, W., Langereis, C.G., Abels, H.A., Dai, S., Fang, X., 2007. Tibetan plateau aridification linked to global cooling at the Eocene–Oligocene transition. *Nature* 445, 633–638.
- Fan, J.-J., Wang, Q., Li, J., Wei, G.-J., Ma, J.-L., Ma, L., Li, Q.-W., Jiang, Z.-Q., Zhang, L., Wang, Z.-L., Zhang, L., 2021. Boron and molybdenum isotopic fractionation during crustal anatexis: constraints from the Conadong leucogranites in the Himalayan Block, South Tibet. *Geochim. Cosmochim. Acta* 297, 120–142.
- Förster, M.W., Prelević, D., Schmück, H.R., Buhre, S., Veter, M., Mertz-Kraus, R., Foley, S.F., Jacob, D.E., 2017. Melting and dynamic metasomatism of mixed harzburgite +glimmerite mantle source: implications for the genesis of orogenic potassic magmas. *Chem. Geol.* 455, 182–191.
- Genske, F.S., Turner, S.P., Beier, C., Chu, M.-F., Tonarini, S., Pearson, N.J., Haase, K.M., 2014. Lithium and boron isotope systematics in lavas from the Azores islands reveal crustal assimilation. *Chem. Geol.* 373, 27–36.
- Goussin, F., Riel, N., Cordier, C., Guillot, S., Boulvais, P., Roperch, P., Replumaz, A., Schulmann, K., Dupont-Nivet, G., Rosas, F., Guo, Z., 2020. Carbonated inheritance in the eastern tibetan lithospheric mantle: petrological evidences and geodynamic implications. *Geochem. Geophys. Geosyst.* 21 (e2019GC008495).
- Guillot, S., Hattori, K., Agard, P., Schwartz, S., Vidal, O., 2009. Exhumation processes in oceanic and continental subduction contexts: a review. *Subduction Zone Geodynamics*. Springer, pp. 175–205.
- Guo, Z., Wilson, M., 2012. The Himalayan leucogranites: constraints on the nature of their crustal source region and geodynamic setting. *Gondwana Res.* 22, 360–376.
- Guo, Z., Wilson, M., Liu, J., Mao, Q., 2006. Post-collisional, potassic and ultrapotassic magmatism of the northern Tibetan Plateau: constraints on characteristics of the mantle source, geodynamic setting and uplift mechanisms. *J. Petrol.* 47, 1177–1220.
- Guo, Z., Wilson, M., Zhang, M., Cheng, Z., Zhang, L., 2013. Post-collisional, K-rich mafic magmatism in South Tibet: constraints on Indian slab-to-wedge transport processes and plateau uplift. *Contrib. Mineral. Petro.* 165, 1311–1340.
- Guo, Z., Wilson, M., Zhang, L., Zhang, M., Cheng, Z., Liu, J., 2014. The role of subduction channel mélanges and convergent subduction systems in the petrogenesis of post-collisional K-rich mafic magmatism in NW Tibet. *Lithos* 198, 184–201.
- Guo, Z., Wilson, M., Zhang, M., Cheng, Z., Zhang, L., 2015. Post-collisional ultrapotassic mafic magmatism in South Tibet: products of partial melting of pyroxenite in the mantle wedge induced by roll-back and delamination of the subducted Indian continental lithosphere slab. *J. Petrol.* 56, 1365–1406.
- Hart, S.R., 1984. A large-scale isotope anomaly in the Southern Hemisphere mantle. *Nature* 309, 753–757.
- Hermann, J., Rubatto, D., 2009. Accessory phase control on the trace element signature of sediment melts in subduction zones. *Chem. Geol.* 265, 512–526.
- Hermann, J., Zheng, Y.-F., Rubatto, D., 2013. Deep fluids in subducted continental crust. *Elements* 9, 281–287.
- Hoskin, P., Black, L., 2000. Metamorphic zircon formation by solid state recrystallization of protolith igneous zircon. *J. Metamorph. Geol.* 18, 423–439.
- Ingalls, M., Rowley, D.B., Currie, B., Colman, A.S., 2016. Large-scale subduction of continental crust implied by India–Asia mass-balance calculation. *Nat. Geosci.* 9, 848–853.
- Ishikawa, T., Tera, F., Nakazawa, T., 2001. Boron isotope and trace element systematics of the three volcanic zones in the Kamchatka arc. *Geochim. Cosmochim. Acta* 65, 4523–4537.
- Johnson, M.C., Plank, T., 2000. Dehydration and melting experiments constrain the fate of subducted sediments. *Geochim. Geophys. Geosyst.* 1.
- Kaliwoda, M., Marschall, H.R., Marks, M.A., Ludwig, T., Altherr, R., Markl, G., 2011. Boron and boron isotope systematics in the peralkaline Ilímaussaq intrusion (South Greenland) and its granitic country rocks: a record of magmatic and hydrothermal processes. *Lithos* 125, 51–64.
- Kapp, P., Yin, A., Harrison, T.M., Ding, L., 2005. Cretaceous-Tertiary shortening, basin development, and volcanism in Central Tibet. *Bull. Geol. Soc. Am.* 117, 865–878.
- Kind, R., Yuan, X., Saul, J., Nelson, D., Sobolev, S., Mechle, J., Zhao, W., Kosarev, G., Ni, J., Achauer, U., 2002. Seismic images of crust and upper mantle beneath Tibet: evidence for Eurasian plate subduction. *Science* 298, 1219–1221.
- Leeman, W.P., Tonarini, S., Turner, S., 2017. Boron isotope variations in Tonga-Kermadec-New Zealand arc lavas: implications for the origin of subduction components and mantle influences. *Geochem. Geophys. Geosyst.* 18, 1126–1162.
- Li, Y., Wang, C., Dai, J., Xu, G., Hou, Y., Li, X., 2015. Propagation of the deformation and growth of the Tibetan–Himalayan orogen: a review. *Earth Sci. Rev.* 143, 36–61.
- Liu, X.-M., Rudnick, R.L., 2011. Constraints on continental crustal mass loss via chemical weathering using lithium and its isotopes. *Proc. Natl. Acad. Sci.* 108, 20873–20880.
- Liu, X., O'Neill, H.S.C., Berry, A.J., 2006. The effects of small amounts of  $\text{H}_2\text{O}$ ,  $\text{CO}_2$  and  $\text{Na}_2\text{O}$  on the partial melting of spinel lherzolite in the system  $\text{CaO}-\text{MgO}-\text{Al}_2\text{O}_3-\text{SiO}_2 \pm \text{H}_2\text{O} \pm \text{CO}_2 \pm \text{Na}_2\text{O}$  at 1–1 GPa. *J. Petrol.* 47, 409–434.
- Liu, W., Yang, Y., Busigny, V., Xia, Q.-K., 2019. Intimate link between ammonium loss of phengite and the deep Earth's water cycle. *Earth Planet. Sci. Lett.* 513, 95–102.
- Long, X., Wilde, S.A., Wang, Q., Yuan, C., Wang, X.-C., Li, J., Jiang, Z., Dan, W., 2015. Partial melting of thickened continental crust in Central Tibet: evidence from geochemistry and geochronology of Eocene adakitic rhyolites in the northern Qiangtang Terrane. *Earth Planet. Sci. Lett.* 414, 30–44.
- Ma, L., Wang, Q., Li, Z.-X., Wyman, D.A., Yang, J.-H., Jiang, Z.-Q., Liu, Y.-S., Gou, G.-N., Guo, H.-F., 2017. Subduction of Indian continent beneath southern Tibet in the latest Eocene (~35 Ma): insights from the Quguosha gabbros in southern Lhasa block. *Gondwana Res.* 41, 77–92.
- Ma, L., Wang, Q., Kerr, A.C., Tang, G.-J., 2021. Nature of the pre-collisional lithospheric mantle in Central Tibet: insights to Tibetan Plateau uplift. *Lithos* 388–389, 106076 (<https://doi.org/10.101016/j.lithos.102021.106076>).
- Marschall, H.R., Foster, G.L., 2018. Boron isotopes in the earth and planetary sciences—A short history and introduction. In: Marschall, H., Foster, G. (Eds.), *Boron Isotopes: The Fifth Element*. Springer International Publishing, Cham, pp. 1–11.
- Marschall, H.R., Schumacher, J.C., 2012. Arc magmas sourced from mélange diapirs in subduction zones. *Nat. Geosci.* 5, 862–867.
- Marschall, H.R., Altherr, R., Rüpkle, L., 2007. Squeezing out the slab—modelling the release of Li, Be and B during progressive high-pressure metamorphism. *Chem. Geol.* 239, 323–335.
- Marschall, H.R., Wanless, V.D., Shimizu, N., von Strandmann, P.A.P., Elliott, T., Monteleone, B.D., 2017. The boron and lithium isotopic composition of mid-ocean ridge basalts and the mantle. *Geochim. Cosmochim. Acta* 207, 102–138.
- Menold, C.A., Grove, M., Sievers, N.E., Manning, C.E., Yin, A., Young, E.D., Ziegler, K., 2016. Argon, oxygen, and boron isotopic evidence documenting 40Ar/39Ar accumulation in phengite during water-rich high-pressure subduction metasomatism of continental crust. *Earth Planet. Sci. Lett.* 446, 56–67.
- Mitchell, A.L., Grove, T.L., 2015. Melting the hydrous subarc mantle: the origin of primitive andesites. *Contrib. Mineral. Petro.* 170, 13. (<https://doi.org/10.1007/s00410-0015-0116-00414>).
- Muttik, N., Kirsimäe, K., Newsom, H.E., Williams, L.B., 2011. Boron isotope composition of secondary smectite in suevites at the Ries crater, Germany: Boron fractionation in weathering and hydrothermal processes. *Earth Planet. Sci. Lett.* 310, 244–251.
- Nielsen, S.G., Marschall, H.R., 2017. Geochemical evidence for mélange melting in global arcs. *Sci. Adv.* 3, e1602402.
- Ou, Q., Wang, Q., Wyman, D.A., Zhang, H.X., Yang, J.H., Zeng, J.P., Hao, L.L., Chen, Y.W., Liang, H., Qi, Y., 2017. Eocene adakitic porphyries in the central-northern Qiangtang Block, Central Tibet: partial melting of thickened lower crust and implications for initial surface uplifting of the plateau. *J. Geophys. Res. Solid Earth* 122, 1025–1053.
- Ou, Q., Wang, Q., Wyman, D.A., Zhang, C., Hao, L.-L., Dan, W., Jiang, Z.-Q., Wu, F.-Y., Yang, J.-H., Zhang, H.-X., 2019. Postcollisional delamination and partial melting of enriched lithospheric mantle: evidence from Oligocene (ca. 30 Ma) potassium-rich lavas in the Gemuchaka area of the central Qiangtang Block, Tibet. *Geol. Soc. Am. Bull.* 131, 1385–1408.
- Palmer, M.R., 2017. Boron cycling in subduction zones. *Elements* 13, 237–242.
- Palmer, M., Ersoy, E.Y., Akal, C., Uysal, I., Genç, S., Banks, L., Cooper, M., Milton, J., Zhao, K., 2019. A short, sharp pulse of potassium-rich volcanism during continental collision and subduction. *Geology* 47, 1079–1082.
- Peng, Y., Yu, S., Li, S., Liu, Y., Santos, M., Lv, P., Li, Y., Xie, W., Liu, Y., 2020. The odyssey of Tibetan Plateau accretion prior to Cenozoic India–Asia collision: probing the Mesozoic tectonic evolution of the Bangong–Nujiang Suture. *Earth Sci. Rev.* 211, 103376.
- Romer, R.L., Meixner, A., Hahne, K., 2014. Lithium and boron isotopic composition of sedimentary rocks—the role of source history and depositional environment: a 250 Ma record from the Cadomian orogeny to the Variscan orogeny. *Gondwana Res.* 26, 1093–1110.
- Rose, E.F., Chaussidon, M., France-Lanord, C., 2000. Fractionation of boron isotopes during erosion processes: the example of Himalayan rivers. *Geochim. Cosmochim. Acta* 64, 397–408.
- Royden, L.H., Burchfiel, B.C., van der Hilst, R.D., 2008. The geological evolution of the Tibetan Plateau. *Science* 321, 1054–1058.
- Rudnick, R., Gao, S., 2014. Composition of the continental crust. *Treatise on Geochemistry*, second ed., pp. 1–51.
- Ryan, J.G., Chauvel, C., 2014. The subduction-zone filter and the impact of recycled materials on the evolution of the mantle. In: Holland, H.D., Turekian, K.K. (Eds.), *Treatise on Geochemistry*, Second ed. Elsevier, pp. 479–508.
- Ryan, J.G., Leeman, W.P., Morris, J.D., Langmuir, C.H., 1996. The boron systematics of intra-plate lavas: implications for crust and mantle evolution. *Geochim. Cosmochim. Acta* 60, 415–422.
- Schmidt, M.W., Poli, S., 1998. Experimentally based water budgets for dehydrating slabs and consequences for arc magma generation. *Earth Planet. Sci. Lett.* 163, 361–379.
- She, Z., Ma, C., Mason, R., Li, J., Wang, G., Lei, Y., 2006. Provenance of the Triassic Songpan–Ganzi flysch, West China. *Chem. Geol.* 231, 159–175.

- Smith, H.J., Spivack, A.J., Staudigel, H., Hart, S.R., 1995. The boron isotopic composition of altered oceanic crust. *Chem. Geol.* 126, 119–135.
- Spurlin, M.S., Yin, A., Horton, B.K., Zhou, J., Wang, J., 2005. Structural evolution of the Yushu-Nangqian region and its relationship to syncollisional igneous activity, east-Central Tibet. *Geol. Soc. Am. Bull.* 117, 1293–1317.
- Stepanov, A.S., Hermann, J., Rubatto, D., Rapp, R.P., 2012. Experimental study of monazite/melt partitioning with implications for the REE, Th and U geochemistry of crustal rocks. *Chem. Geol.* 300, 200–220.
- Stern, R.J., 2002. Subduction zones. *Rev. Geophys.* 40, 1012. <https://doi.org/10.1029/2001RG000108>.
- Sun, S.S., McDonough, W., 1989. Chemical and isotopic systematics of oceanic basalts: implications for mantle composition and processes. *Geol. Soc. Lond., Spec. Publ.* 42, 313–345.
- Tanaka, R., Nakamura, E., 2005. Boron isotopic constraints on the source of Hawaiian shield lavas. *Geochim. Cosmochim. Acta* 69, 3385–3399.
- Tappognier, P., Zhiqin, X., Roger, F., Meyer, B., Arnaud, N., Wittlinger, G., Jingsui, Y., 2001. Oblique stepwise rise and growth of the Tibet Plateau. *Science* 294, 1671–1677.
- Tatsumi, Y., 2006. High-Mg andesites in the Setouchi volcanic belt, southwestern Japan: analogy to Archean magmatism and continental crust formation? *Annu. Rev. Earth Planet. Sci.* 34, 467–499.
- Tatsumi, Y., Eggins, S.M., 1995. Subduction Zone Magmatism. Blackwell, Cambridge.
- Tomanikova, L., Savov, I.P., Harvey, J., de Hoog, J.C., Churikova, T.G., Gordeychik, B., Yodogzinski, G.M., 2019. A limited role for metasomatized subarc mantle in the generation of boron isotope signatures of arc volcanic rocks. *Geology* 47, 517–521.
- Tonarini, S., Leeman, W.P., Leat, P.T., 2011. Subduction erosion of forearc mantle wedge implicated in the genesis of the South Sandwich Island (SSI) arc: evidence from boron isotope systematics. *Earth Planet. Sci. Lett.* 301, 275–284.
- Trumbull, R.B., Slack, J.F., 2018. Boron isotopes in the continental crust: granites, pegmatites, felsic volcanic rocks, and related ore deposits. In: Marschall, H., Foster, G. (Eds.), *Boron Isotopes*. Springer, Cham, pp. 249–272.
- Turner, S., Hawkesworth, C., Liu, J.Q., Rogers, N., Kelley, S., Van Calsteren, P., 1993. Timing of Tibetan uplift constrained by analysis of volcanic rocks. *Nature* 364, 50–54.
- Turner, S., Arnaud, N., LIU, J., Rogers, N., Hawkesworth, C., Harris, N., Kelley, S.v., Van Calsteren, P., Deng, W., 1996. Post-collision, shoshonitic volcanism on the Tibetan Plateau: implications for convective thinning of the lithosphere and the source of ocean island basalts. *J. Petrol.* 37, 45–71.
- Turner, S., Tonarini, S., Bindeman, I., Leeman, W.P., Schaefer, B.F., 2007. Boron and oxygen isotope evidence for recycling of subducted components over the past 2.5 Gyr. *Nature* 447, 702–705.
- van Hinsbergen, D.J.J., Steinberger, B., Doubrovine, P.V., Gassmöller, R., 2011. Acceleration and deceleration of India-Asia convergence since the cretaceous: roles of mantle plumes and continental collision. *J. Geophys. Res. Solid Earth* 116.
- Wang, C., Liu, Z., Yi, H., Liu, S., Zhao, X., 2002. Tertiary crustal shortening and peneplanation in the Hoh Xil region: implications for the tectonic history of the northern Tibetan Plateau. *J. Asian Earth Sci.* 20, 211–223.
- Wang, Q., Wyman, D.A., Xu, J., Dong, Y., Vasconcelos, P.M., Pearson, N., Wan, Y., Dong, H., Li, C., Yu, Y., Zhu, T., Feng, X., Zhang, Q., Zi, F., Chu, Z., 2008. Eocene melting of subducting continental crust and early uplifting of Central Tibet: evidence from central-western Qiangtang high-K calc-alkaline andesites, dacites and rhyolites. *Earth Planet. Sci. Lett.* 272, 158–171.
- Wang, Q., Wyman, D.A., Li, Z.-X., Sun, W., Chung, S.-L., Vasconcelos, P.M., Zhang, Q., Dong, H., Yu, Y., Pearson, N., 2010. Eocene north-south trending dikes in Central Tibet: new constraints on the timing of east-west extension with implications for early plateau uplift? *Earth Planet. Sci. Lett.* 298, 205–216.
- Wang, Q., Hawkesworth, C.J., Wyman, D., Chung, S.-L., Wu, F.-Y., Li, X.-H., Li, Z.-X., Gou, G.-N., Zhang, X.-Z., Tang, G.-J., 2016. Pliocene-Quaternary crustal melting in central and northern Tibet and insights into crustal flow. *Nat. Commun.* 7, 11888. <https://doi.org/10.11038/ncomms11888>.
- Wang, Y., Foley, S.F., Prelević, D., 2017. Potassium-rich magmatism from a phlogopite-free source. *Geology* 45, 467–470.
- Wei, G., Wei, J., Liu, Y., Ke, T., Ren, Z., Ma, J., Xu, Y., 2013. Measurement on high-precision boron isotope of silicate materials by a single column purification method and MC-ICP-MS. *J. Anal. At. Spectrom.* 28, 606–612.
- Wiedenbeck, M., Alle, P., Corfu, F., Griffin, W., Meier, M., Oberli, F.v., Quadt, A.v., Roddick, J., Spiegel, W., 1995. Three natural zircon standards for U-Th-Pb, Lu-Hf, trace element and REE analyses. *Geostand. Newslett.* 19, 1–23.
- Workman, R.K., Hart, S.R., 2005. Major and trace element composition of the depleted MORB mantle (DMM). *Earth Planet. Sci. Lett.* 231, 53–72.
- Xu, W., Liu, F., Dong, Y., 2020. Cambrian to Triassic geodynamic evolution of central Qiangtang, Tibet. *Earth Sci. Rev.* 201, 103083.
- Yakovlev, P.V., Saal, A., Clark, M.K., Hong, C., Niemi, N.A., Mallick, S., 2019. The geochemistry of Tibetan lavas: spatial and temporal relationships, tectonic links and geodynamic implications. *Earth Planet. Sci. Lett.* 520, 115–126.
- Yin, A., Harrison, T.M., 2000. Geologic evolution of the Himalayan-Tibetan orogen. *Annu. Rev. Earth Planet. Sci.* 28, 211–280.
- Zack, T., Foley, S.F., Rivers, T., 2002. Equilibrium and disequilibrium trace element partitioning in hydrous eclogites (Trescolmen, Central Alps). *J. Petrol.* 43, 1947–1974.
- Zhang, P.-Z., Shen, Z., Wang, M., Gan, W., Bürgmann, R., Molnar, P., Wang, Q., Niu, Z., Sun, J., Wu, J., Hanrong, S., Xinzhaoy, Y., 2004. Continuous deformation of the Tibetan Plateau from global positioning system data. *Geology* 32, 809–812.
- Zhao, J., Yuan, X., Liu, H., Kumar, P., Pei, S., Kind, R., Zhang, Z., Teng, J., Ding, L., Gao, X., 2010. The boundary between the Indian and Asian tectonic plates below Tibet. *Proc. Natl. Acad. Sci.* 107, 11229–11233.
- Zhao, W., Kumar, P., Mechie, J., Kind, R., Meissner, R., Wu, Z., Shi, D., Su, H., Xue, G., Karplus, M., 2011. Tibetan plate overriding the Asian plate in central and northern Tibet. *Nat. Geosci.* 4, 870–873.
- Zheng, Y.-F., 2012. Metamorphic chemical geodynamics in continental subduction zones. *Chem. Geol.* 328, 5–48.
- Zhu, D.-C., Zhao, Z.-D., Niu, Y., Dilek, Y., Hou, Z.-Q., Mo, X.-X., 2013. The origin and pre-Cenozoic evolution of the Tibetan Plateau. *Gondwana Res.* 23, 1429–1454.